



# MID-AMERICA TRANSPORTATION CENTER

Report # MATC-MS&T: 125-1

Final Report

WBS: 25-1121-0005-125-1



## Earthquake-Induced Damage Classification of Bridges Using Artificial Neural Network

**Genda Chen, PhD, PE**

Professor and Robert W Abbett Distinguished  
Chair in Civil Engineering  
Department of Civil, Architectural, and  
Environmental Engineering  
Missouri University of Science and Technology

**Ibrahim Alomari**

PhD Student  
Department of Civil, Architectural, and  
Environmental Engineering

**Woubishet Taffese**

Post-doctoral Fellow  
Center for Intelligent Infrastructure  
Department of Civil, Architectural, and  
Environmental Engineering

**Mohammad Hossein  
Afsharmovahed**

PhD Student  
Department of Civil, Architectural, and  
Environmental Engineering



2024

A Cooperative Research Project sponsored by  
U.S. Department of Transportation- Office of the Assistant  
Secretary for Research and Technology

The contents of this report reflect the views of the authors, who are responsible for the facts and the accuracy of the information presented herein. This document is disseminated in the interest of information exchange. The report is funded, partially or entirely, by a grant from the U.S. Department of Transportation's University Transportation Centers Program. However, the U.S. Government assumes no liability for the contents or use thereof.

MATC

# Earthquake-induced Damage Classification of Bridges Using Artificial Neural Network

Genda Chen, Ph.D., P.E.  
Professor and Robert W. Abbett  
Distinguished Chair in Civil Engineering  
Department of Civil, Architectural, and  
Environmental Engineering  
Missouri University of Science and  
Technology

Woubishet Taffese, Post-doctoral Fellow  
Center for Intelligent Infrastructure  
Department of Civil, Architectural, and  
Environmental Engineering  
Missouri University of Science and  
Technology

Ibrahim Alomari, Ph.D. Student  
Department of Civil, Architectural, and  
Environmental Engineering  
Missouri University of Science and  
Technology

Mohammad Hossein Afsharmovahed, Ph.D.  
Student  
Department of Civil, Architectural, and  
Environmental Engineering  
Missouri University of Science and  
Technology

A Report on Research Sponsored by

Mid-America Transportation Center

University of Nebraska–Lincoln

June 30, 2024

## Technical Report Documentation Page

1. Report No. 25-1121-0005-125-1	2. Government Accession No.	3. Recipient's Catalog No.	
4. Title and Subtitle Earthquake-induced Damage Classification of Bridges Using Artificial Neural Network		5. Report Date September 2024	
		6. Performing Organization Code Missouri S&T	
7. Author(s) Genda Chen, Ibrahim Alomari, Woubishet Taffese, Mohammad Hossein Afsharmovahed		8. Performing Organization Report No. 25-1121-0005-125-1	
9. Performing Organization Name and Address Center for Intelligent Infrastructure Department of Civil, Architectural, and Environmental Engineering Missouri University of Science and Technology 500 W. 16 <sup>th</sup> St. Rolla, MO 65409-0810		10. Work Unit No. ()	
		11. Contract or Grant No. 69A3551747107	
12. Sponsoring Agency Name and Address Mid-America Transportation Center 2200 Vine St. PO Box 830851 Lincoln, NE 68583-0851		13. Type of Report and Period Covered Final Report January 2021 – June 2024	
		14. Sponsoring Agency Code MATC TRB RiP# 91994-85	
15. Supplementary Notes			
16. Abstract Ensuring the resilience of bridges against earthquakes is crucial for the rapid recovery of communities. Speedy and accurate damage assessments are essential for pinpointing the most affected areas and facilitating prompt decision-making. Current methods (i.e., fragility curves and estimates) are often slow and inaccurate. To address these issues, we developed a novel damage evaluation model for highway bridges using two three-layer Artificial Neural Network (ANN) models: A and B. These models predict earthquake-induced bridge damage levels (none, slight, moderate, extensive, and collapse) of a particular type of bridges based on intensity measures from historical ground motion records. Key highway bridges were selected for modeling, and their damage states were assessed using a damage index through nonlinear time history analysis (NLTHA). This generated a comprehensive dataset for training, validating, and testing the ANN models. Our approach significantly outperforms traditional fragility estimations by offering rapid and accurate damage predictions. Model A and Model B achieved 90.74% and 95.43% accuracies, respectively. This improved accuracy enhances immediate response efforts and supports proactive decision-making, thereby bolstering earthquake preparedness and resilience.			
17. ORCID No. of each Researcher Genda Chen: 0000-0002-0658-4356		18. Distribution Statement	
19. Security Classif. (of this report) Unclassified	20. Security Classif. (of this page) Unclassified	21. No. of Pages 77	22. Price

## TABLE OF CONTENTS

List of Figures .....	iv
List of Tables .....	vi
Acknowledgments.....	vii
Disclaimer .....	viii
Executive Summary .....	ix
Chapter 1 Introduction .....	1
1.1 Research motivation.....	1
1.2 Research objectives and significance.....	4
1.3 Framework for developing for ANN earthquake damage assessment model.....	5
Chapter 2 Bridge Selection and Ground Motion Collection.....	7
2.1 Selection of representative highway bridges .....	7
2.1.1 The A1466 Bridge.....	9
2.1.2 The L472 Bridge .....	15
2.2 Collecting ground motions records .....	20
Chapter 3 Finite Element Modelling and NLTHA .....	22
3.1 Finite element model.....	22
3.1.1 Material models .....	22
3.1.2 Superstructure element models .....	23
3.1.3 Foundation model .....	27
3.2 Nonlinear static pushover analysis.....	41
3.3 Dynamic characteristics of the L472 and A1466 bridges .....	42
3.4 Nonlinear time history analysis .....	43
Chapter 4 Data Processing .....	44
4.1 Damage indices and classification. ....	44
4.2 Intensity measures.....	46
4.3 Correlation and ranking of IMs.....	55
Chapter 5 ANN seismic classifier.....	64
5.1 ANN seismic classifier methodology .....	64
5.2 Classification model (A).....	68
5.3 Classification model (B) .....	71
Chapter 6 Conclusions .....	74
References.....	75



## List of Figures

Figure 1.1 Observed collapses in different bridges resulting from 1994 north (Cooper, James, and I. Friedland 1994).....	2
Figure 1.2 Framework for earthquake damage assessment model development using (ANNs)....	6
Figure 2.1: Earthquake hazard map of the U.S based on (USGS 2018).....	7
Figure 2.2 Pemiscot County spotlighted on the Missouri county map, designated for this research project .....	8
Figure 2.3 Satellite images of the A1466 Bridge site .....	9
Figure 2.4 Elevation view of the A1466 Bridge .....	10
Figure 2.5 A1466 Twin Bridges (real image).....	11
Figure 2.6 Plan showing foundations (bents and abutments) of the A1466 Bridge .....	11
Figure 2.7 Structural steel plan of the A1466 Bridge .....	11
Figure 2.8 Cross-sectional view the diaphragm of the A1466 Bridge.....	12
Figure 2.9 Bent details of the A1466 Bridge (a concrete cap supported by two columns) .....	13
Figure 2.10 Footing plan with piles configurations of the A1466 Bridge .....	14
Figure 2.11 Abutment Details of the A1466 Bridge (supported by eight piles).....	14
Figure 2.12 Satellite images of the L472 Bridge site.....	15
Figure 2.13 The general elevation layout of the L472 Bridge.....	16
Figure 2.14 The elevation view (real image) of the L472 Bridge .....	17
Figure 2.15 Plan showing foundations (bents and piles) of the L472 Bridge.....	17
Figure 2.16 Structural steel plan view of the L472 Bridge deck .....	18
Figure 2.17 Cross-section of end and intermediate diaphragms of the L472 Bridge .....	19
Figure 2.18 Intermediate bent details of the L472 Bridge (a concrete cap supported by three columns).....	20
Figure 3.1 Stress-strain diagrams: (a) tensile behavior of steel materials and (b) compressive behavior of concrete materials .....	23
Figure 3.2 Computational model of the superstructure .....	24
Figure 3.3 RC fiber sections details.....	25
Figure 3.4 Hysteric behavior of RC shear spring .....	25
Figure 3.5 The details of the steel fiber sections .....	26
Figure 3.6 Pounding spring and expansion joints models .....	27
Figure 3.7 Computational foundation model details.....	28
Figure 3.8 p-y models of soft clay (Matlock 1970), sand (API's 1993).....	30
Figure 3.9 p-multipliers with maximum horizontal acceleration relationship.....	35
Figure 3.10 8-piles group configuration in bridge A1466 .....	35
Figure 3.11 TzSimple1 Material used in this study .....	36
Figure 3.12 Nonlinear static pushover analysis for (A1466 and L472) bridges.....	41
Figure 4.1 Correlation ranking of IMs based on maximum drift ratios.....	59
Figure 4.2: Most important IMs ranked based on <b>R2</b> .....	60
Figure 4.3 Correlation plot between <i>PGA</i> scalar and directional values with <i>MDR</i> .....	61
Figure 4.4 Correlation plot between spectral accelerations at vibration periods with <i>MDR</i> .....	63
Figure 5.1 The architecture of the ANN seismic classifier using IMs as inputs and damage states resulted from NLTHA as output .....	64
Figure 5.2 Details of the data used in Model (A) showing training, validation, and testing datasets. ....	68

Figure 5.3 Confusion matrices of Model (A) where green and red cells are the percentages of right and wrong classifications in the current subset. ....	70
Figure 5.4 Details of the data used in Model (B) showing training, validation, and testing datasets. ....	71
Figure 5.5 Confusion matrices of Model (B) where green and red cells are the percentages of right and wrong classifications in the current subset. ....	73

## List of Tables

Table 3.1 p-y model parameters of the clay layers at the L472 Bridge site (Chen et al. 2005)....	31
Table 3.2 p-y model parameters of the sand layers at the L472 Bridge site (Chen et al. 2005)...	32
Table 3.3 p-y model parameters of the clay layers at the A1466 Bridge site (Chen et al. 2005) .	33
Table 3.4 p-y model parameters of the sand layers at the A1466 bridge site (Chen et al. 2005) .	34
Table 3.5 $\tau$ -z parameters of the soil springs at the L472 Bridge site (Chen et al. 2005) .....	37
Table 3.6 $\tau$ -z parameters of the soil springs at the A1466 Bridge site (Chen et al. 2005).....	38
Table 3.7 q-z parameters for (L472 and A1466) bridges (Chen et al. 2005).....	39
Table 3.8 Damping coefficients used in the bridge models (Chen et al. 2005).....	40
Table 3.9 Vibration Modes periods of (A1466 and L472) bridges.....	42
Table 4.1 Definition of the limit states according to HAZUS (Emergency Management Agency 2022) .....	44
Table 4.2 Correlation between damage indices and damage classifications .....	46
Table 4.3 Definitions and equations of the IMs used in this study.....	49
Table 4.4 IMs with the maximum and minimum values (resultant, x, y and z) components.....	53
Table 4.5 Correlation results of IMs.....	56

## Acknowledgments

We appreciate Dr. Tarutal Ghosh Mondal for his valuable discussion with the project team at the very beginning of this project.

## Disclaimer

The contents of this report reflect the views of the authors, who are responsible for the facts and the accuracy of the information presented herein. This document is disseminated in the interest of information exchange. The report is funded, partially or entirely, by a grant from the U.S. Department of Transportation's University Transportation Centers Program. However, the U.S. Government assumes no liability for the contents or use thereof.

## Executive Summary

Ensuring the protection of bridges from natural hazards, particularly earthquakes, is critical for the rapid response and recovery of communities and cities. Effective earthquake damage assessment is essential for identifying the most affected areas and facilitating immediate attention and decision-making. Current methods need significant improvements in speed and accuracy to meet these demands. To address this need, a novel, rapid, and accurate damage evaluation model for highway bridges was developed using two three-layer Artificial Neural Network (ANN) models: A and B. These models forecast the seismic damage levels of a particular type of bridges based on various intensity measures derived from past ground motion records. The damage levels are classified into five categories: none, slight, moderate, extensive, and collapse. The development process begins with selecting representative bridges along major highways and collecting a comprehensive dataset of ground motions. These bridges are then modeled, and their damage states are assessed using a damage index through nonlinear time history analysis (NLTHA). The ground motions are labeled with the corresponding damage states to create a balanced training, validation, and test dataset for the ANN. This ANN-based classifier offers a significant advancement over traditional fragility estimations by providing rapid and accurate damage predictions. The proposed models that are more accurate than traditional fragility estimations enhance immediate response efforts and support proactive decision-making, potentially improving earthquake preparedness and resilience.

## Chapter 1 Introduction

### 1.1 Research motivation

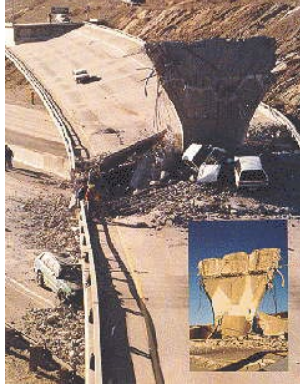
Bridges serve as critical nodes in ground transportation networks, playing a pivotal role in infrastructure operations and safety. Protecting bridges from severe damage caused by natural hazards, such as earthquakes, is of paramount importance. According to the United States Geological Survey (USGS), bridges have recently been subjected to an increasing number of significant seismic events. Notably, since 1990, there have been over 28 earthquakes worldwide with magnitudes ranging from 7.6 to 9.1 (USGS, 2016). Additionally, of the 20 largest recorded earthquakes, seven have occurred after 2001. In 2010 alone, 23 major earthquakes, with magnitudes of 7.0 or greater, were recorded.

According to (NCEER-94-0008), during the Northridge earthquake in 1994, seven highway bridges experienced partial collapses, and an additional 170 bridges sustained damage, ranging from minor cracking to the slumping of abutment fills. Figure 1.1 illustrates three incidents resulting from this earthquake:

(a) I-5 SR 14 Interchange: Three spans collapsed due to the complete crushing of one column and the failure of prestressed steel tendons through the column cap of a standing column.

(b) Santa Monica Freeway (I-10): A section of the westbound freeway between Venice Boulevard and La Cienega collapsed. The failure was attributed to the pre-1971 column design. This structure was scheduled for column retrofitting in February 1994.

(c) Golden State Freeway (I-5) - Antelope Valley Freeway (State Route 14) Interchange: One of the two connector structures collapsed, with two spans failing due to the crushing of a column. The photograph shows the superstructure shear failure resulting from the column collapse.



(a) I-5 SR 14 interchange



(b) Santa Monica Freeway (I-10)



(c) Golden State Freeway (I-5)

Figure 1.1 Observed collapses in different bridges resulting from 1994 north (Cooper, James, and I. Friedland 1994)

In the face of increasing seismic activity, the concept of seismic resilience has become essential in disaster management. Seismic resilience refers to the ability of communities, buildings, infrastructure, and systems to withstand, respond to, and recover from seismic events. This capability is essential for minimizing casualties, reducing economic losses, and ensuring the continuity of services. To apply the concept of seismic resilience in practice, rapid post-earthquake response and recovery for communities and cities are essential. However, achieving this is challenging, if not impossible, without a rapid and effective damage evaluation approach to identify the areas most affected by an earthquake.



Fragility analysis is a key tool in seismic evaluation, providing a probabilistic assessment of a structure's vulnerability to seismic events (Yasmin et al. 2015). It is particularly useful in assessing the performance of structural systems, taking into account uncertainties and randomness (Krishna and Gopi 2017). Current approaches to fragility analysis utilize various measures of seismic intensity, known as intensity measures (IM), such as peak ground acceleration and pseudo spectral acceleration (Kafali and Grigoriu 2007).

The fragility analysis method has been found to produce results with substantial errors. Román-De La Sancha et al. (2019) evaluated the reliability of seismic fragility models by comparing predicted damage with observed damage at a site severely affected by the September 19th, 2017, Puebla-Mexico City earthquake. They discovered that the observed extensive damage to concrete and masonry buildings exceeded the predicted damage by approximately 20–30. Karamlou and Bocchini (2015) determined that the assumption of a lognormal distribution is a source of errors in seismic-induced damage calculations. Ciano, Gioffrè, and Grigoriu (2020) demonstrated that the accuracy and variability of fragility curves depend on the selected intensity measures, which can vary significantly between scalar and vector-valued intensity measures. Mangalathu, Heo, and Jeon (2018) trained an artificial neural network (ANN) using structural parameters and intensity measures as input neurons to establish a multi-dimensional probabilistic seismic demand model (PSDM). This model was based on dynamic analyses of skewed concrete bridges under 320 ground motion records. Yuan et al. (2022) developed multivariate seismic classifiers with multiple intensity measures as inputs for a four-story building utilizing ANNs to address the limitations of traditional regression approaches.

Based on recent findings, it is crucial to develop more accurate and rapid methods for earthquake damage assessments. Enhancing these methods can provide more precise evaluations of structural damage, ensuring that the most affected areas receive immediate attention post-earthquake. Furthermore, improved assessment techniques can aid in proactive decision-making regarding bridges, enhancing both immediate response efforts and future earthquake preparedness.

### 1.2 Research objectives and significance.

The primary objective is to develop artificial neural networks (ANNs) for real-time evaluation of structural damage in highway bridges following an earthquake. This study aims to create a more rapid and precise method than fragility curves by using ANNs as ground motion classifiers for direct damage state evaluation. By optimizing these ANNs for robust and accurate performance, the study seeks to provide a reliable tool for immediate post-earthquake assessment. Improving the accuracy and speed of damage evaluations will enhance community resilience and safety. Delayed and inaccurate damage assessments can significantly hamper emergency response efforts. Rescue teams might be dispatched to less affected areas while severely damaged regions are overlooked. This misallocation of resources can lead to prolonged suffering, increased fatalities, and further structural damage due to delayed interventions.

The development and implementation of ANNs for real-time evaluation of earthquake damage to bridges carry several significant benefits:

1. Implementation: Applying the trained ANNs to real-world bridge networks for practical assessment and decision-making.

2. **Timely Decision-Making:** Enabling rapid and informed decisions in the aftermath of an earthquake by quickly identifying the most affected areas and prioritizing rescue operations.
3. **Minimizing Delays:** Reducing the hours or even days needed for traditional assessments, allowing for immediate action and timely interventions.
4. **Efficiency:** Using ANNs to quickly analyze data and provide faster assessment results. Additionally, data from future earthquakes can further refine the ANN models, improving their predictive capabilities.
5. **Scalability:** ANNs can be applied to multiple bridges and regions, making them versatile tools for widespread use in earthquake-prone areas. Since many highway bridges are built to similar specifications, representative bridges can be used to develop ANN models applicable to other bridges with similar characteristics.

### 1.3 Framework for developing for ANN earthquake damage assessment model.

To create a rapid and highly precise damage evaluation classification model applicable to a wide range of highway bridges, two three-layer ANN models were constructed. The ground motion classifier model forecasts the potential damage levels for bridges during earthquakes based on various scalar and vector-valued intensity measures derived from past unscaled and scaled ground motion records. These damage levels are categorized into five distinct classes: none, slight, moderate, extensive, and collapse.

The framework for conducting this study is depicted in Figure 1.2. It begins with the selection of representative bridges along major highways, followed by the collection and organization of a comprehensive dataset of ground motions. Subsequently, the representative bridges are modeled, and their damage states are assessed based on a damage index under the

ground motions through nonlinear time history analysis (NLTHA). The ground motions are then labeled with corresponding damage states, and a balanced set of training and test data is developed. Next, the ANN is trained using the training dataset, and the overall accuracy of damage prediction is evaluated. Finally, the ANN architecture is optimized for robust and accurate performance by prioritizing the importance of various intensity measures, comparing structural damage indices, and exploring different configurations of hidden layers and neurons.

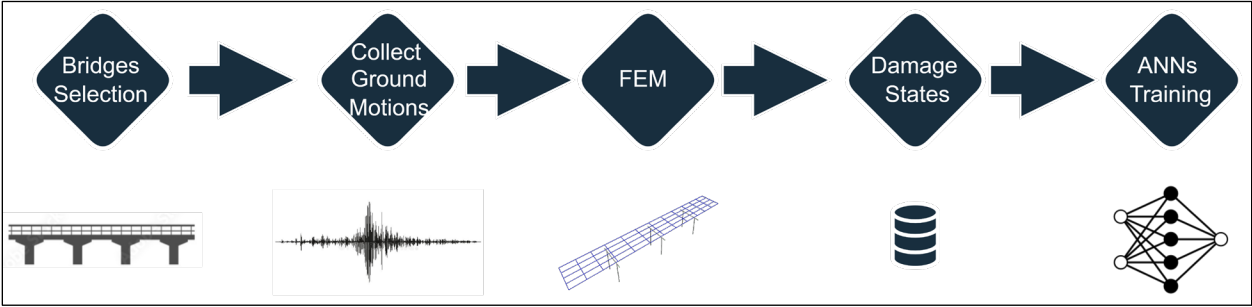


Figure 1.2 Framework for earthquake damage assessment model development using (ANNs)

## Chapter 2 Bridge Selection and Ground Motion Collection

### 2.1 Selection of representative highway bridges

Numerous bridges along a single highway are grouped together and constructed using similar processes and materials, aiming to minimize design and construction expenses. For instance, spanning approximately 64 kilometers, there are nine four-span bridges over the I-44, sharing nearly identical layouts: three are steel-girder bridges, and six are concrete solid deck bridges. Consequently, this study will focus on training ANNs for earthquake damage classification using two representative bridges from steel-girder bridges.

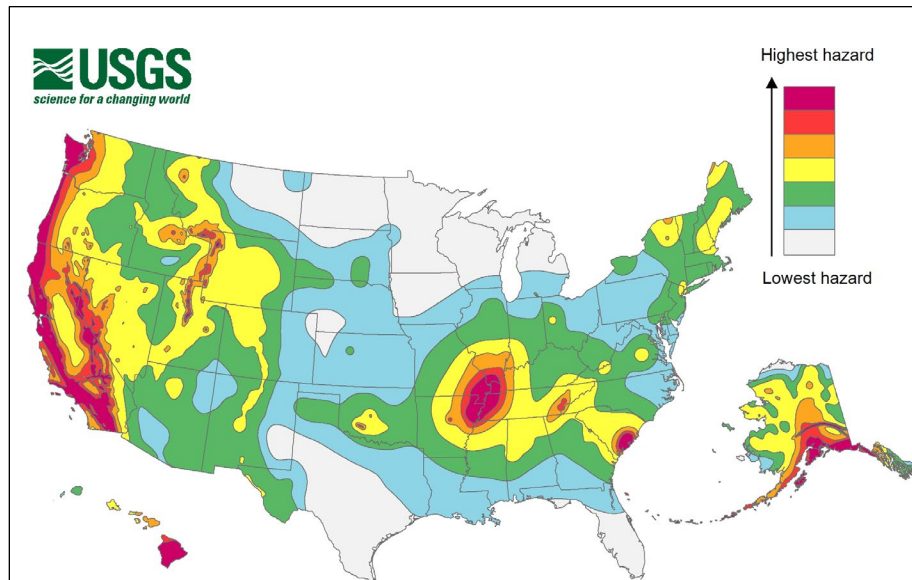


Figure 2.1: Earthquake hazard map of the U.S based on (USGS 2018)

Figure 2.1 presented an earthquake hazard map depicting peak ground accelerations with a two percent probability of occurrence over a 50-year span (USGS, 2018). This map utilized the latest USGS models for the contiguous United States (2018), Hawaii (1998), and Alaska (2007).

Notably, the map highlights areas of highest seismic risk predominantly along the western coast and in the new Madrid seismic zone comprising Missouri, Illinois, Kentucky, Tennessee, and Arkansas. The selection of two bridges situated within the highest hazard zone in southeast Missouri's Pemiscot County was informed by this map, as depicted in Figure 2.2.

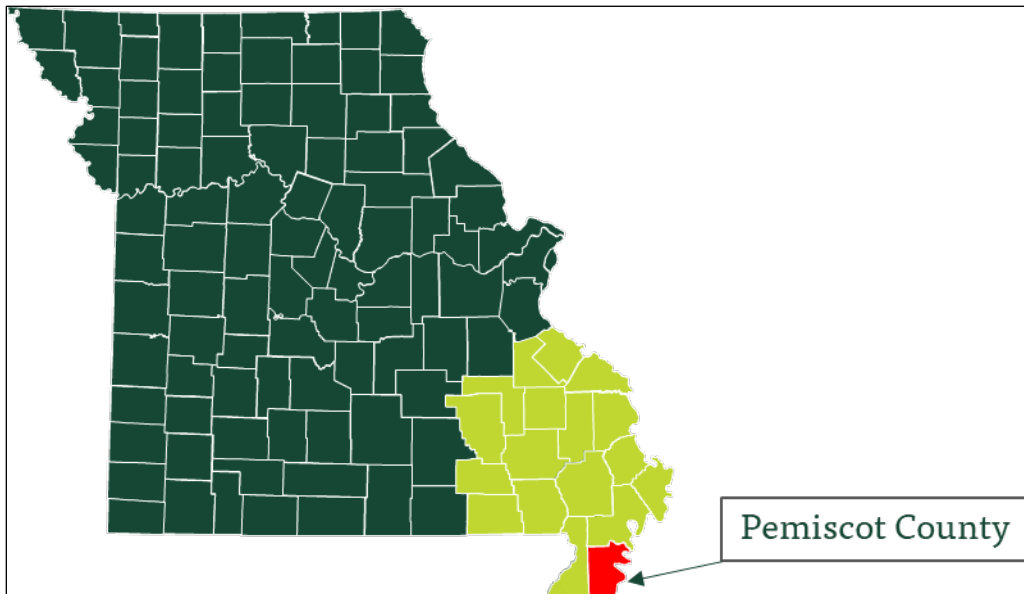


Figure 2.2 Pemiscot County spotlighted on the Missouri county map, designated for this research project

The two bridges selected for this study, designed in the 1950s-1960s, were designed according to old versions of AASHTO specifications, which did not account for seismic considerations. The first bridge is A-1466, and the second bridge is L472. These bridges were selected as representative examples of the highway infrastructure. As typical highway bridges in the central United States, they provide a relevant case study for assessing seismic vulnerability. The bridges represent different design ages, materials, and configurations, allowing the study to evaluate a range of highway bridge types.

### 2.1.1 The A1466 Bridge

The A1466 twin bridges, designed in 1966 according to 1965 AASHTO specifications, locate over railway tracks and a county road along Interstate Highway I-55, about 4.8 km (3.0 miles) southeast of Hayti in Pemiscot County. Satellite imagery of the A1466 site is depicted in Figure 2.3. Its geographic coordinates are approximately (89.740° W, 36.220° N). The longitudinal axis of the bridges sits at an angle of around 12° measured counterclockwise from the orientation of the southwestern segment.

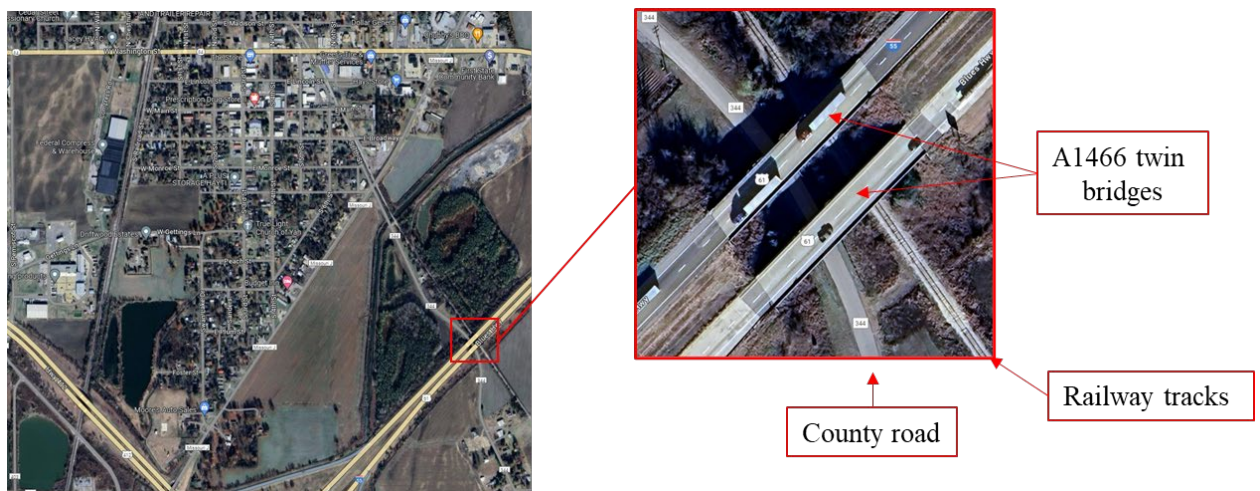


Figure 2.3 Satellite images of the A1466 Bridge site

Each bridge within the A1466 twin structure accommodates two traffic lanes, with a total length of 74.8 m (245 ft 5¼ in.). The width of each roadway spans 11.4 m (37.5 ft). Both bridges are skewed by 10.5° and consist of four spans of continuous steel girder construction. Each bridge consists of three bents and two abutments. The distance between the twin bridges measures 12.8 m (42 ft) center to center. Span lengths vary: 16.68 m (54 ft 8⅝ in.), 20.72 m (68 ft), 20.72 m (68 ft), and 16.68 m (54 ft 8⅝ in.) between abutment 1 and bent 2, bents 2–3, bents

3–4, and bent 4 and abutment 5, respectively. Figure 2.4 illustrates the general elevation side view layout of the A1466 bridge.

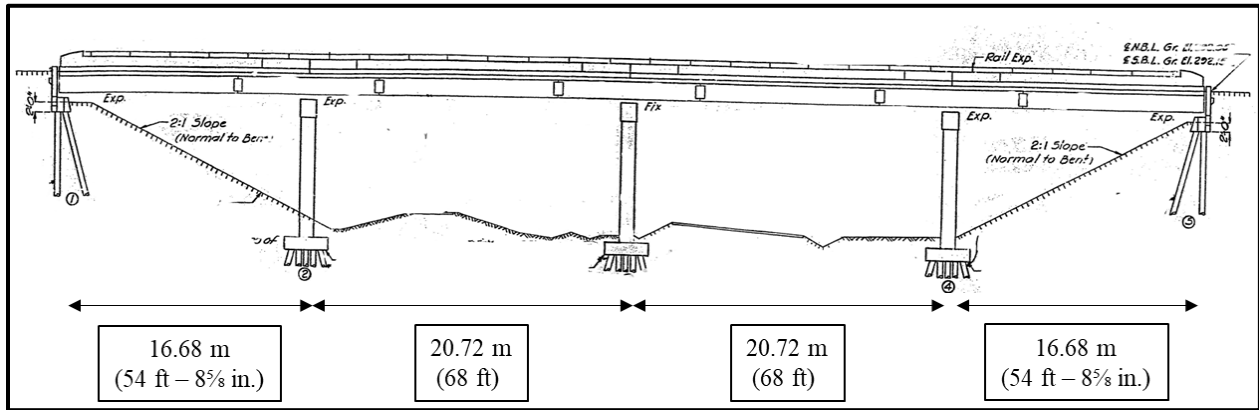


Figure 2.4 Elevation view of the A1466 Bridge

The 0.19 m (7½ in.) reinforced concrete deck is supported on continuous steel girders, restrained laterally by end diaphragms (at the location of each bent) and intermediate diaphragms (between bents), as shown in Figure 2.4. The superstructure is supported by three intermediate bents and two abutments utilizing type ‘D’ fixed and expansion steel bearings. Each intermediate bent comprises a reinforced concrete cap beam supported by two reinforced concrete columns. The real image of A1466 bridges is shown in Figure 2.5. Pile foundations of length 12.2 m (40 ft) support all bents and each column is supported by a pile cap carried by 8 piles, totaling 16 piles per bent. The abutments are supported by cast-in-place concrete pile foundations of length 18.3 m (60 ft). each abutment is supported by 8 piles as shown in figure 2.6.





Figure 2.5 A1466 Twin Bridges (real image)

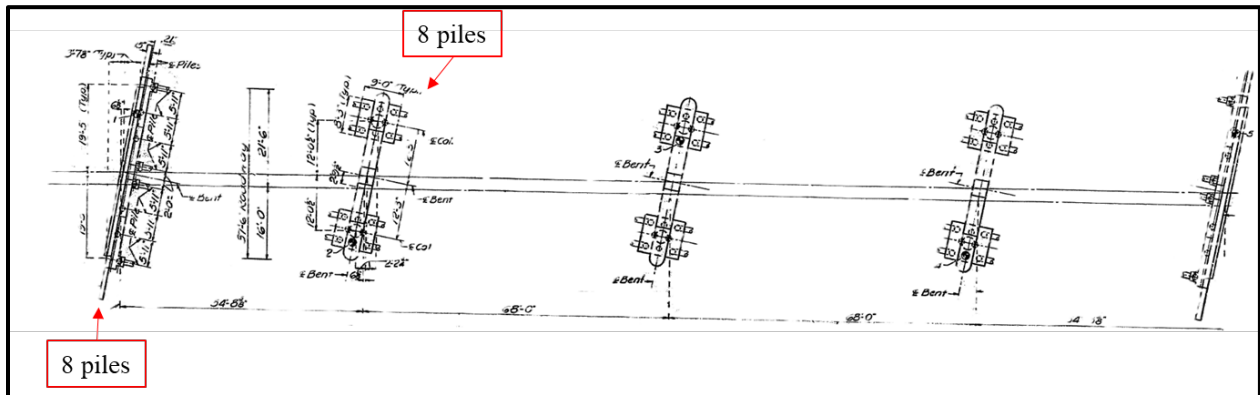


Figure 2.6 Plan showing foundations (bents and abutments) of the A1466 Bridge

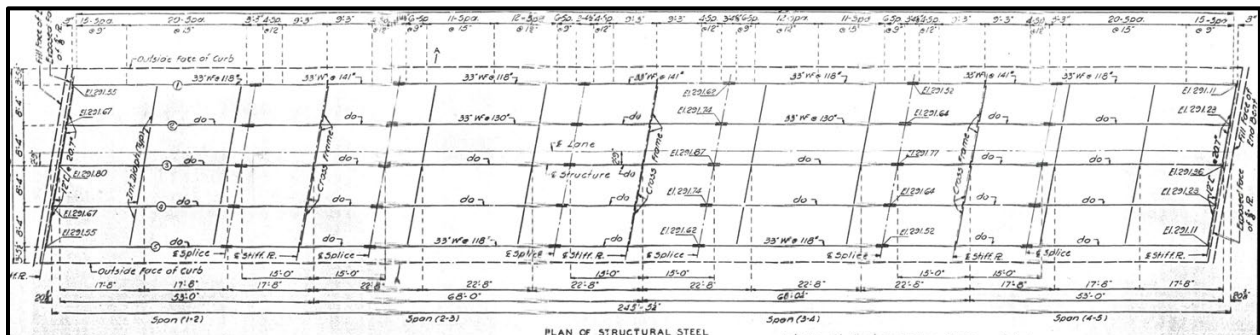


Figure 2.7 Structural steel plan of the A1466 Bridge

Figure 2.7 and 2.8 presents the structural steel plan for bridge A1466 and the cross-sectional view of the diaphragm, illustrating the use of wide flange sections as major girders and C-sections as minor beams. The major girders consist of W33x118, W33x130, and W33x141 sections, while the minor beams are C12x20.7 sections. The elevation points are shown in Figure 2.7, with specific assignments at the intersection points.

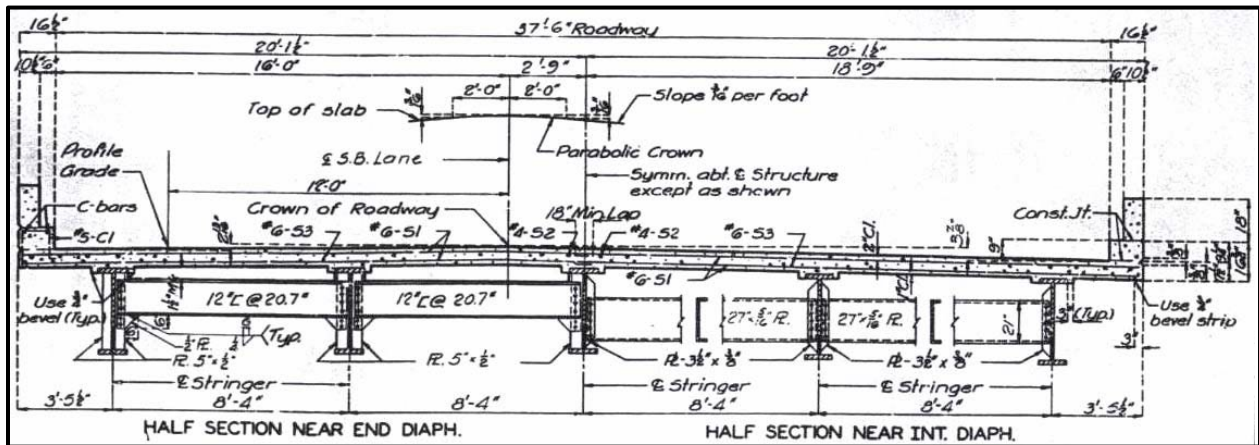


Figure 2.8 Cross-sectional view the diaphragm of the A1466 Bridge

The concrete cap beam measures 0.965 m (3 ft 2 in.) in width, 1.143 m (3 ft 9 in.) in depth and spans a total length of 11.38 m (37 ft 4 in.). It is reinforced with 9 #10 bars at the bottom, 5 #7 bars at the top, and 4 additional #8 bars at the beam ends.

The columns in the intermediate bents have a circular cross-section with a diameter of 0.91 m (3 ft) and a total length of 7.44 m (24 ft 5 in.). They are reinforced longitudinally with eight #10 bars and transversely with #3 bars spaced at 0.30 m (12 in.).

The concrete compressive strength utilized in both beams and columns is 24.13 MPa (or 3.5 ksi) and reinforcement details are Grade 40, yield strength 276 MPa (40 ksi).



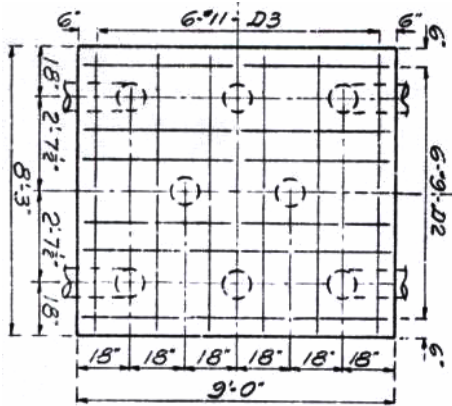


Figure 2.10 Footing plan with piles configurations of the A1466 Bridge

The rectangular part of the abutment's cross-section is 0.762 m (2 ft 6 in.) wide, 0.91 m (3 ft) high, with a total length of 17.5 m (57 ft 1 in.). It is reinforced with four #7 bars at the top and bottom. Each abutment is supported by eight piles, with details shown in Figure 2.11.

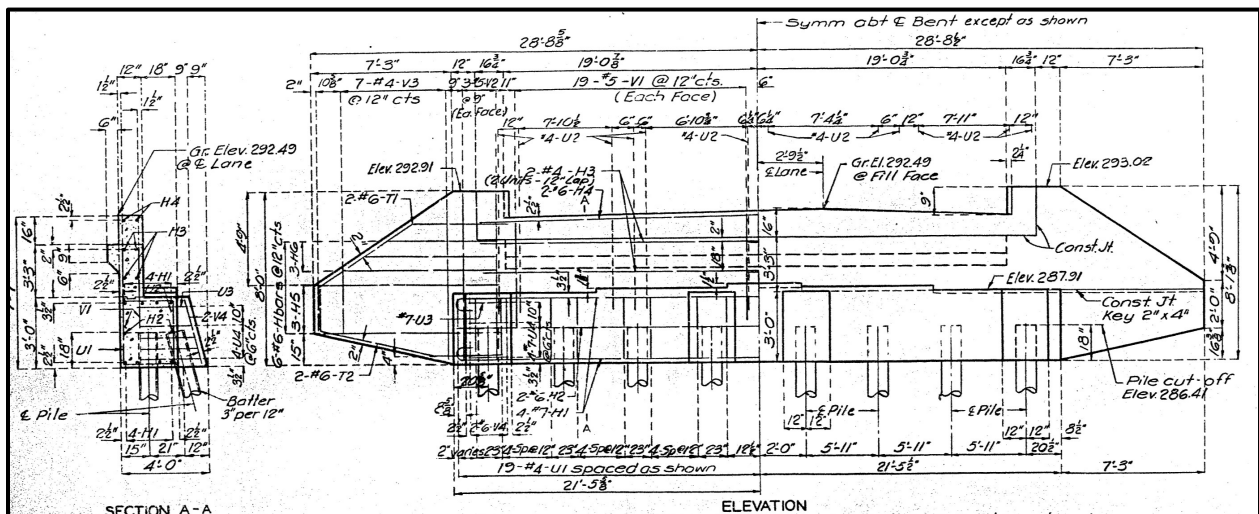


Figure 2.11 Abutment Details of the A1466 Bridge (supported by eight piles)



### 2.1.2 The L472 Bridge

Bridge L472 comprises twin bridges designed in 1952 according to the 1949 AASHTO specifications, lacking seismic considerations. Located over Ditch #3 on Interstate Highway I-55, approximately 5.6 km (3.5 miles) northeast of Steele in Pemiscot County, the bridge's geographic coordinates are approximately (89.780° W, 36.100° N). The longitudinal axis of the bridges is oriented at an angle of about 15° counterclockwise from the southwestern segment. Each bridge accommodates two traffic lanes, with a total length of 57 m (187 ft). The roadway was widened in 1971 to 11.6 m (38 ft), and the deck was repaired in 1984. Satellite imagery of the L472 bridge site is depicted in figure 2.12.



Figure 2.12 Satellite images of the L472 Bridge site

The L472 bridges are skewed by 57° and consist of five spans of continuous steel girders. Span lengths are: 10.78 m (35 ft 4½ in.), 10.17 m (33 ft 4¼ in.), 15.1 m (49 ft 6½ in.), 10.17 m (33 ft 4¼ in.), and 10.78 m (35 ft 4½ in.) respectively. Figure 2.13 illustrates the general elevation side view layout of the L472 bridge.

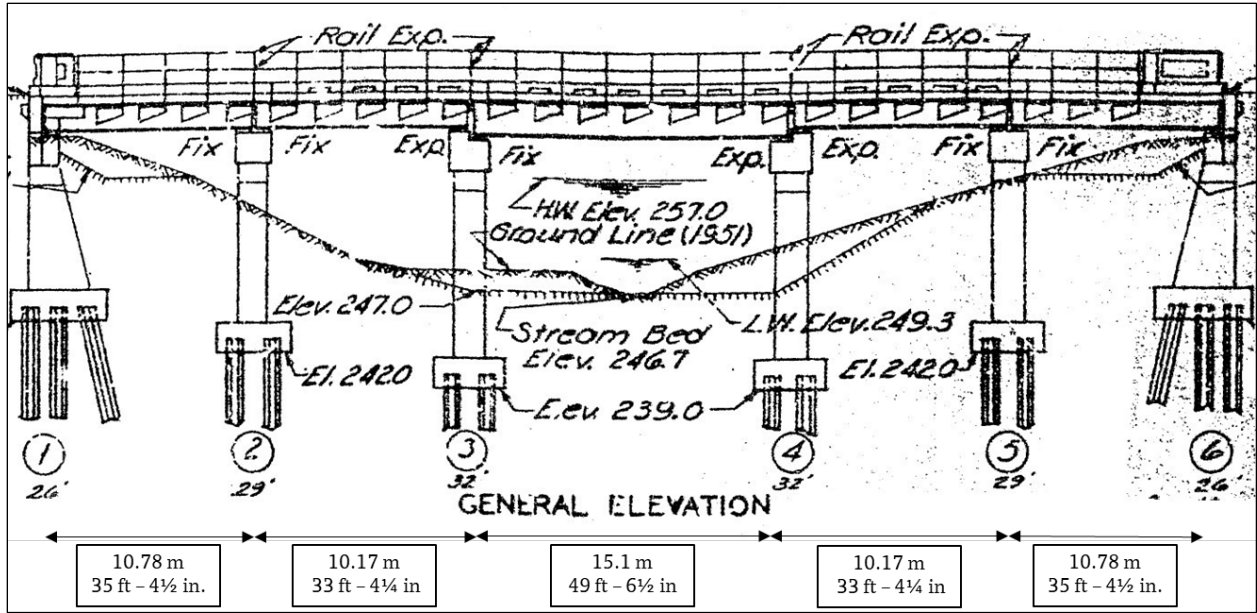


Figure 2.13 The general elevation layout of the L472 Bridge

The 0.17 m (6 1/2 in.) reinforced concrete deck is supported by continuous steel girders, which are laterally restrained by end diaphragms (located at each bent) and intermediate diaphragms (situated between bents), as illustrated in Figure 2.13. The superstructure is supported by six bents utilizing type 'C' fixed and expansion steel bearings. Each intermediate bent consists of a reinforced concrete cap beam supported by three reinforced concrete columns. A real image of the L472 bridges is shown in Figure 2.14. Pile foundations, ranging from 7.6 to 9.1 m (25 to 30 ft) in length, support all bents. Each column is supported by a footing, with the number of piles per footing varying: the intermediate columns of the end bents are supported by 5 piles, while the rest are supported by 4 piles, resulting in 12 piles per intermediate bent and 18 piles per end bent, as shown in Figure 2.15.



Figure 2.14 The elevation view (real image) of the L472 Bridge

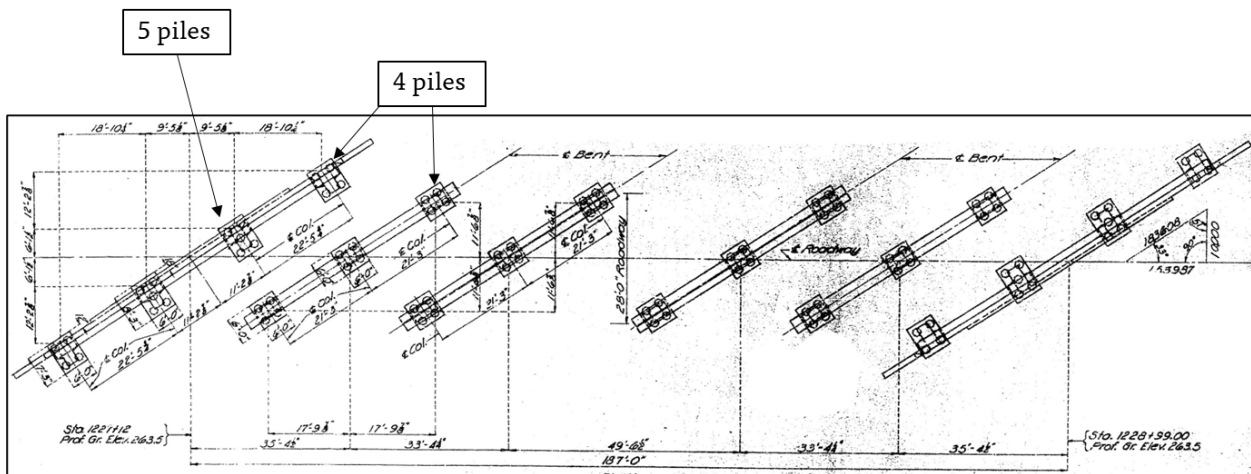


Figure 2.15 Plan showing foundations (bents and piles) of the L472 Bridge

Figure 2.16 presents the structural steel plan for bridge L472 and illustrating the use of wide flange sections as major girders. For the external girders, W27x94 was used for shorter spans and W36x150 was used for the long span, while for the interior girders W27x114 was used for the shorter spans and W36x182 was used for the long span. The steel girders are laterally restrained by end diaphragms at each bent and intermediate diaphragms between bents, as shown in Figure 2.17.

The concrete cap beam is 0.8636 m (2 ft 10 in.) in width, 0.762 m (2 ft 6 in.) in depth and total length of 16.154 m (53 ft) over two 6.477 m (21 ft 3 in.) spans, It is reinforced with six #10





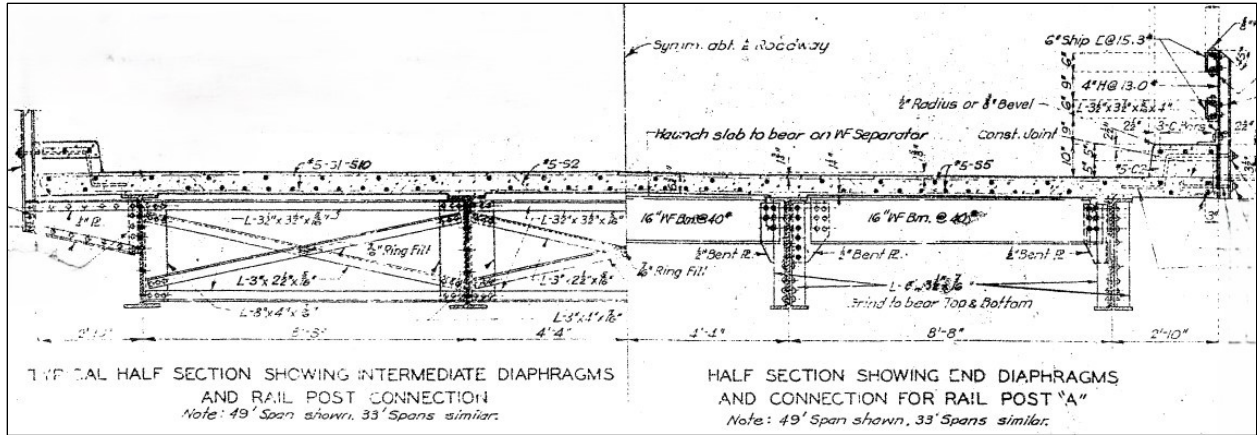


Figure 2.17 Cross-section of end and intermediate diaphragms of the L472 Bridge

The footings have a depth of 0.762 m (2 ft 6 in.) and a 1.83 m x 1.83 m (6 ft. x 6 ft.) plan section. They are reinforced with six #11 bars in the short direction and six #9 bars in the longitudinal direction. #7 bars are employed as dowels to secure the footing-column joints.

Each footing is supported by four piles, depicted in Figure 2.18, which have a circular cross-section with a diameter of 0.41 m (16 in.). The total lengths of these piles are 9 m (29 ft 6 1/2 in) for bents 1, 3, 4 and 6, and 8 m (26 ft 3 in.) for bents 2 and 5. All details regarding the bents, including the concrete cap and column specifications, are illustrated in Figure 2.18.

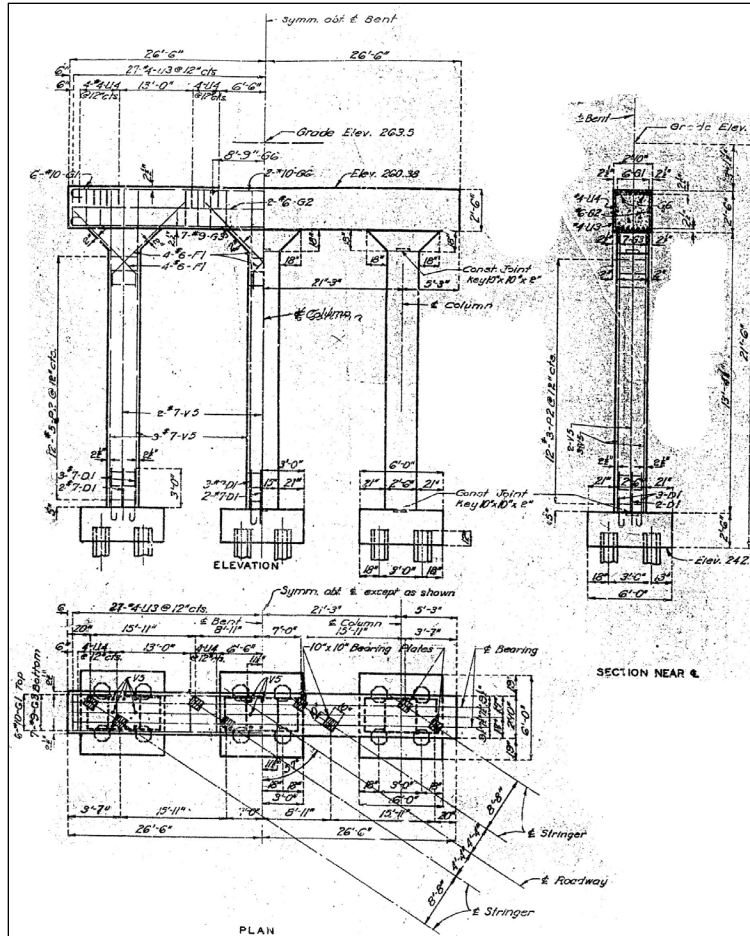


Figure 2.18 Intermediate bent details of the L472 Bridge (a concrete cap supported by three columns)

## 2.2 Collecting ground motions records

A total of 2,093 ground motion records were collected for the nonlinear time history analysis of the two selected bridges. These records, with ground accelerations exceeding  $1.25 \text{ m/s}^2$ , were sourced from the Pacific Earthquake Engineering Research Center (PEER) ground motion database. The earthquakes had magnitudes greater than 6. The selection criteria ensured randomness and variety, encompassing various locations and regions to account for a broad range of seismic activity uncertainties. This approach generated datasets that consider a spectrum

of damage classifications, from weak earthquakes causing no or minor damage to strong earthquakes leading to collapse or severe damage.

The ground motions were scaled by factors ranging from 2 to 10 to produce strong ground motion records that generate a sufficient number of collapse and severe state records. This scaling approach is supported by literature, indicating that realistic records can be obtained when scaled records reach the target pseudo-spectral acceleration level at the fundamental period of the structure. However, it is important to note that excessive scaling can introduce bias into the numerical seismic response. The appropriate scaling limit is a matter of ongoing debate within the engineering seismology community, with acceptable limits varying widely from 2 to 10 or more (Vamvatsikos and Cornell 2002; Luco and Bazzurro 2007; Miano et al. 2018; Elghazouli, Kumar, and Stafford 2014; Kostinakis, Athanatopoulou, and Morfidis 2015; Rathje et al. 2004) .

To minimize excessive scaling and its potential biases, it was found that the induced bias in seismic response also depends on structural properties, intensity, and dynamic responses, as validated by other studies. Consequently, a total of 20,930 acceleration records were generated by scaling the original records from 2 to 10. This dataset will be further classified and used to train artificial neural network models for seismic damage classification.

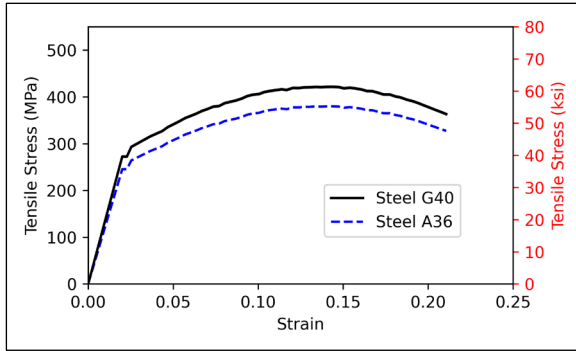
## Chapter 3 Finite Element Modelling and NLTHA

### 3.1 Finite element model

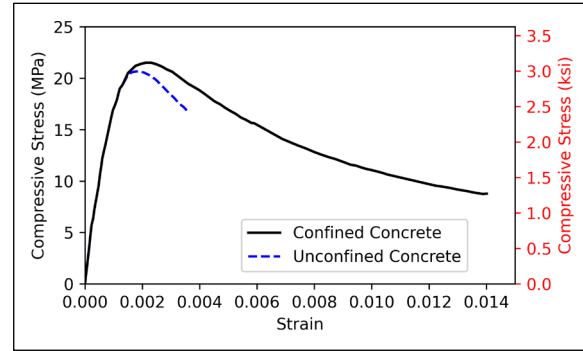
To achieve the nonlinear time history analysis of the two bridges under the action of different ground motions, a finite element model was created. This structural finite element model simulates the response of the bridges under seismic activity. The analysis was performed using the OpenSees (Open System for Earthquake Engineering Simulation) Python library, developed by the Pacific Earthquake Engineering Research Center in 2006.

#### *3.1.1 Material models*

The concrete used in the superstructure was modeled using the Concrete02 model for the unconfined sections around the transverse reinforcement in the concrete beams and columns. For the confined core sections within the transverse reinforcement of the reinforced concrete columns and beams, the ConfinedConcrete01 model was applied. The Steel02 model was utilized to simulate the steel girders and beams, with the steel specified as A36, having a yield strength of 248.2 MPa (36 ksi). Additionally, the Steel02 model was used to simulate the grade 40 reinforcement bars in the concrete columns and beams with a yield strength of 275.8 MPa (40 ksi). Figure 3.1 illustrates the stress-strain diagrams of the material models.



(a) Tensile behavior of steel



(b) Compressive behavior of concrete

Figure 3.1 Stress-strain diagrams: (a) tensile behavior of steel materials and (b) compressive behavior of concrete materials

### 3.1.2 Superstructure element models

The reinforced concrete deck was modeled as elastic shell elements since it is expected to remain elastic during earthquakes. The effective stiffness for reinforced concrete decks is defined as 25% of the gross stiffness, according to ACI 318-19. Displacement-based beam-column elements with fiber-defined cross-sections were used to model the wide flange steel sections, RC beams, and columns. Fiber cross-sections offer the distinct advantage of specifying unique material properties for separate locations across a member's cross-section. Each reinforcing bar was simulated as a fiber, with the concrete area divided into confined and unconfined concrete. The unconfined concrete represents the concrete cover, while the confined concrete refers to the core concrete within the transverse reinforcement. Stresses and strains were computed at each fiber, and each beam-column element was assigned eight integration points along its length to capture nonlinear behavior effectively the RC fiber sections are shown in Figure 3.3 . Zero-length springs were assigned at each end of the RC beam and column elements to account for strength and stiffness degradation resulting from bar slip behavior. Nonlinear springs were used to model shear deformation behavior at the ends of each member using the punching limit state

model, enhancing the accuracy of drift and deflection calculations. The details of the computational model of the superstructure is shown in Figure 3.2.

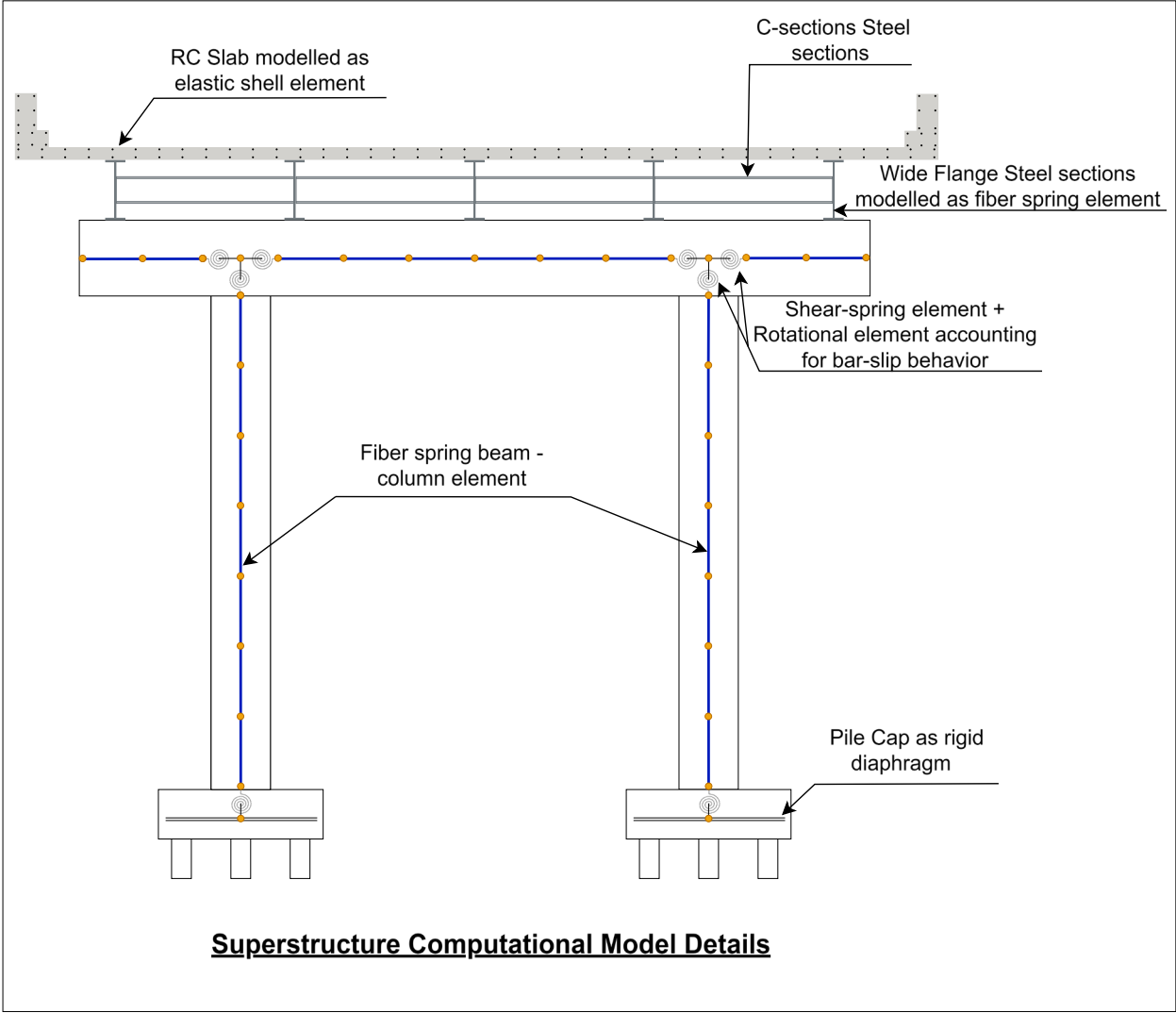


Figure 3.2 Computational model of the superstructure

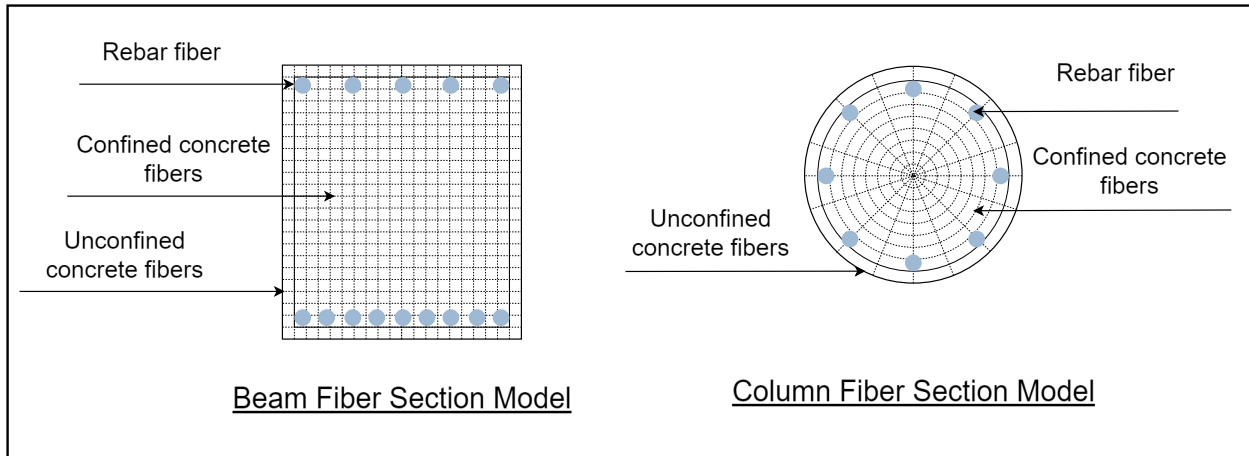


Figure 3.3 RC fiber sections details

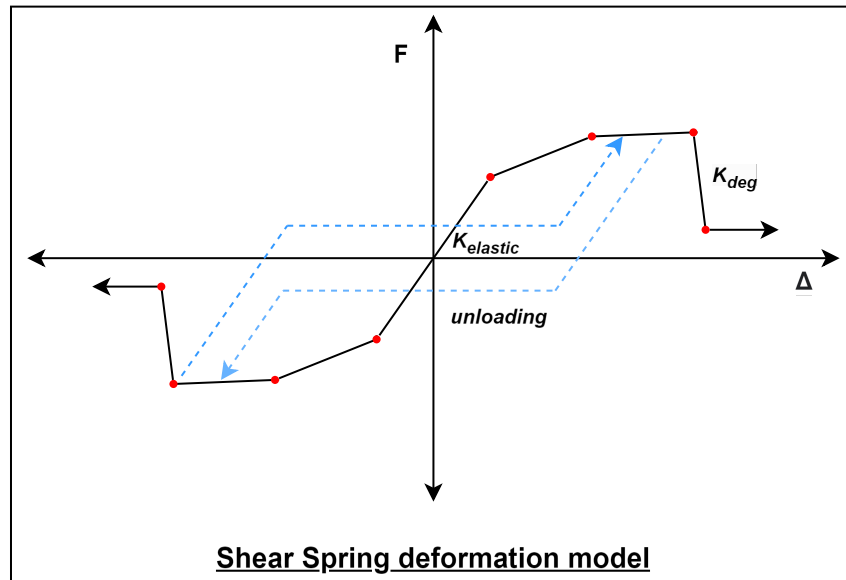


Figure 3.4 Hysteretic behavior of RC shear spring

The wide flange sections were simulated as T-beams, with the effective width of the concrete slab acting as a compression element determined according to AISC specifications. The details of the steel fiber sections are shown in Figure 3.5

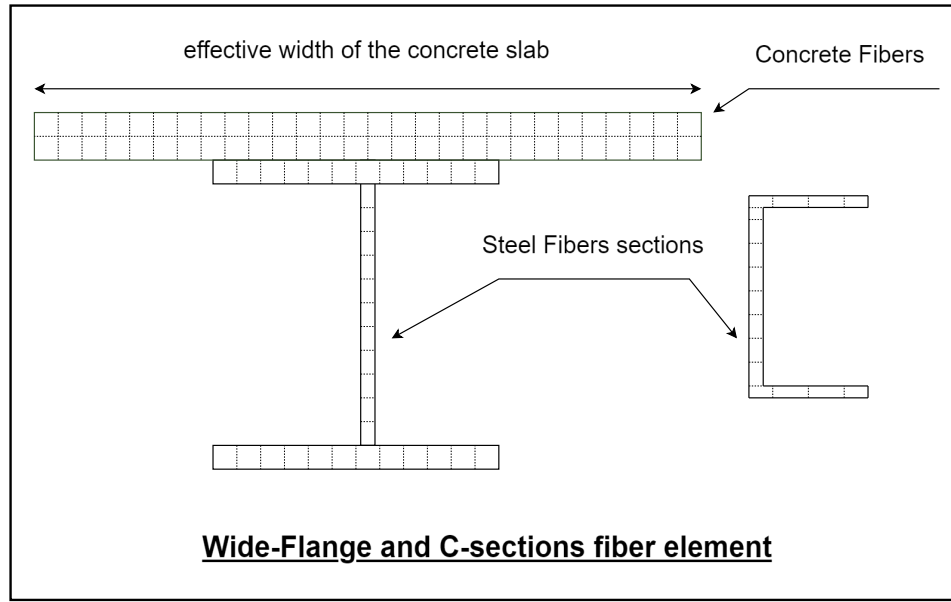


Figure 3.5 The details of the steel fiber sections

Expansion joints, types C and D, were also modeled to account for the effect of bounding between adjacent decks and girders. Type C steel expansion joint bearings were used in Bridge L472, with a clear opening of 0.019 m (3/4 in.) between the anchor bolts and the cap beam, and a slot in the upper plate of each bearing. Type D steel expansion bearings were used in Bridge A1466, allowing for a maximum displacement of 0.036 m (1.435 in.) at the abutments and 0.042 m (1.642 in.) at the intermediate bents. In the finite element model, the expansion joints were modeled using zero-length springs with a gap property. Initially, the stiffness is zero, but when the gap closes, stiffness is introduced. When the displacement exceeds the gap and it reopens, the stiffness returns to zero, continuing the cycle. To accommodate the bounding effect between adjacent decks or between steel girders and abutments, zero-length springs were modeled as impact elements with a gap property. For Bridge L472, the clear gap between two adjacent RC decks was 0.013 m (1/2 in.) at bents 2 and 5, and 0.019 m (3/4 in.) at bents 3 and 4. For Bridge A1466, the clear gap between the steel girder and the abutment is approximately 0.105 m (4 1/4



in.) at abutments 1 and 5. The models used to model the pounding effect and expansion joints are shown in Figure 3.6.

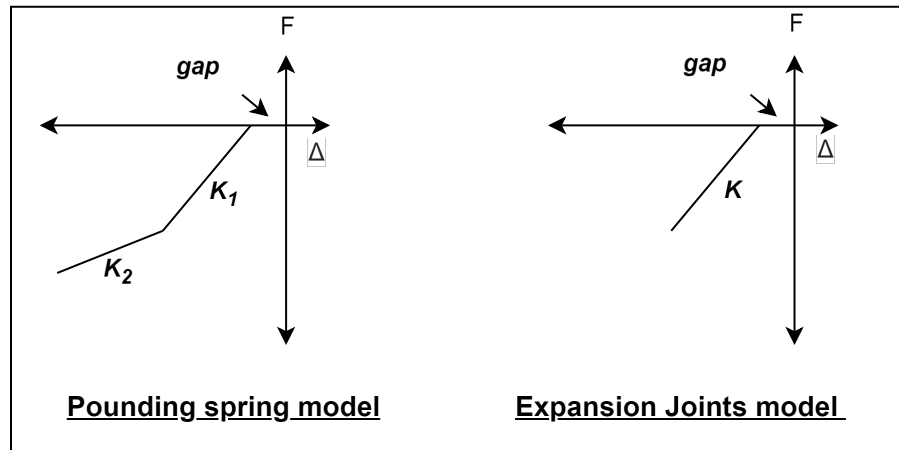


Figure 3.6 Pounding spring and expansion joints models

### 3.1.3 Foundation model

Bridges L472 and A1466 used the pile-soil springs interaction approach for their foundational models. Each pile was modeled as a frame element, while the soil was represented by nonlinear springs. These springs were positioned at equal intervals along the depth of the pile. Each pile cap was modeled as a rigid diaphragm. The nonlinear springs representing the soil were modeled in three orthogonal directions and were located at every joint on each pile. In addition, three corresponding dampers were modeled to account for the damping nature of the soil.

In the lateral direction, hysteretic P-y models, which represent the lateral bearing capacity of the soil, varied with the depth of the pile and were used to model the two lateral horizontal springs. In the vertical direction, hysteretic  $\tau$ -z models, which represent the shear strength between the pile body and the surrounding soil, were used. At the tip end of the pile, hysteretic

Q-z models represent the vertical bearing capacity of the soil on the pile. The details of the foundation model are shown Figure 3.7.

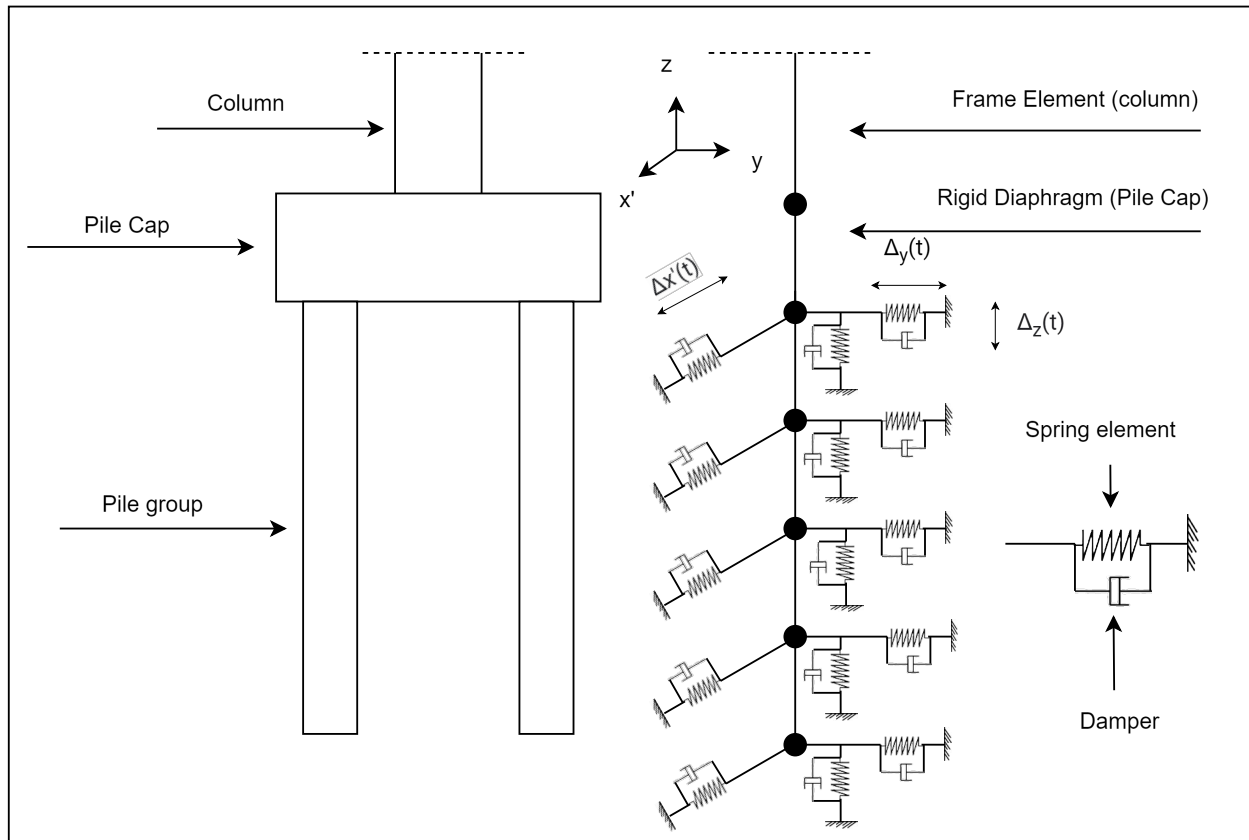


Figure 3.7 Computational foundation model details

The piles group did not work as efficiently as individual piles since they did not take into account P-multipliers were used to modify the p-y behavior. The effect of liquefaction on the soil pile interaction was considered in the A1466 bridge site under the earthquakes that have a magnitude above seven.

### 3.1.3.1 p-y curves model

In OpenSeespy, the PySimple1 material was utilized to simulate the nonlinear behavior of the soil springs. The soft clay model was based on Matlock (1970), while the sand model followed the API (1993) guidelines. The p-y model was represented by three components:

elastic, plastic, and gap components arranged in series. Radiation damping was modeled using a dashpot dependent on the far-field elastic component of the displacement rate (velocity). The gap component consisted of a nonlinear closure spring and a nonlinear drag spring, which operated in parallel. The plastic component of the p-y model is described in equation (3.1), where  $P_{ult}$  represents the ultimate capacity of the distributed load for the pile,  $P_o$  denotes the start of the current plastic loading cycle,  $y_{50}$  is the displacement at which 50% of  $P_{ult}$  is mobilized during monotonic loading, and the constant  $C$  controls the tangent modulus at the onset of plastic yielding, while the exponent  $n$  determines the sharpness of the curve.

$$p = P_{ult} - (P_{ult} - P_o) \left[ \frac{Cy_{50}}{Cy_{50} + |y^p - y_o^p|} \right]^n. \quad (3.1)$$

The closure spring is described by equation (3.2), representing the positive side of the gap. The gap increases on the positive side when plastic deformation occurs on the negative loading side, while the other side of the equation accounts for the rebounding of the gap. This allows for a smooth transition in the load-displacement behavior as the gap opens or closes.

$$p^c = 1.8P_{ult} \left[ \frac{y_{50}}{y_{50} + 50(y_o^+ - y^g)} - \frac{y_{50}}{y_{50} + 50(y_o^- - y^g)} \right]. \quad (3.2)$$

The nonlinear drag spring is described by equation (3.3), where  $C_d$  is the ratio of the maximum drag force to the ultimate capacity. The flexibility of these equations can be utilized to approximate the backbone relationships of the p-y behavior.

$$p^d = C_d p_{ult} - (C_d p_{ult} - p_o^d) \left[ \frac{y_{50}}{y_{50} + 2 |y^g - y_o^g|} \right]^n \quad (3.3)$$

According to Matlock (1970), it is recommended to use the following values for soft clay: ( $C = 10$ ), ( $n = 5$ ) and ( $C_r = 0.35$ ). According to API (1993), it is recommended to use the following values for sand: ( $C = 0.5$ ), ( $n = 2$ ) and ( $C_r = 0.2$ ).

The integration of the elastic, plastic, and gap components simulates the overall p-y model curve. Figure 3.8 displays the two different p-y models: the clay model based on (Matlock 1970) and the sand model based on API (1993).

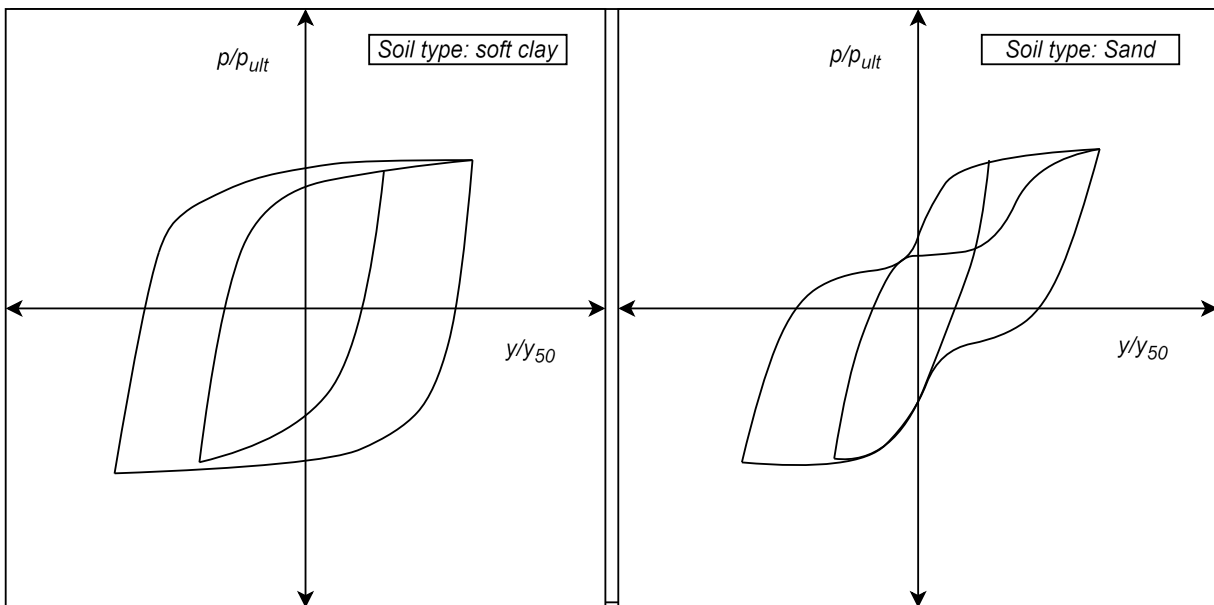


Figure 3.8 p-y models of soft clay (Matlock 1970), sand (API's 1993)

### 3.1.3.2 p-y parameters for the L472 Bridge

All the curves' parameters were based on the Chen et al. (2005) study that was based on the same two bridges. Table 3.1 and 3.2 Shows the parameters of the clay and sand layers respectively such that  $z'$  is the elevations of the springs and  $K_i$  is the initial stiffness of the soil spring.

Table 3.1 p-y model parameters of the clay layers at the L472 Bridge site (Chen et al. 2005)

<b>Bent No.</b>	<b>Spring No.</b>	<b><math>z'</math> (m)</b>	<b>Clay type</b>	<b><math>y_{50}</math> (mm)</b>	<b><math>p_{ult}</math> (kN/m)</b>	<b><math>z_{cr}</math> (m)</b>
1 and 6	1	6.64	medium	8.23	107.5	3.86
2 and 5	1	4.15	medium	8.23	107.5	3.86

Table 3.2 p-y model parameters of the sand layers at the L472 Bridge site (Chen et al. 2005)

Bent No.	Spring No.	$z'$ (m)	Sand type	$E_s$ (kPa)	$k_i$ (kN/m)
1 and 6	2	7.64	medium dense	124400	124400
	3	8.64	medium dense	140700	140700
	4	9.64	medium dense	156900	156900
	5	10.64	medium dense	173200	173200
	6	11.64	medium dense	189500	189500
	7	12.64	dense	428700	428700
	8	13.64	dense	462700	462700
	9	14.64	dense	496600	248300
2 and 5	2	4.65	medium dense	75700	56800
	3	5.65	medium dense	92000	92000
	4	6.65	medium dense	108300	108300
	5	7.65	medium dense	124500	124500
	6	8.65	medium dense	140800	140800
	7	9.65	dense	327300	327300
	8	10.65	dense	361200	361200
	9	11.65	dense	395200	395200
3 and 4	10	12.65	dense	429200	214600
	1	3.44	medium dense	56000	56000
	2	4.44	medium dense	72200	72200
	3	5.44	medium dense	88500	88500
	4	6.44	medium dense	104800	104800
	5	7.44	dense	252300	252300
	6	8.44	dense	286300	286300
	7	9.44	dense	320200	320200
	8	10.44	dense	354100	354100
9	11.44	dense	388000	194000	

### 3.1.3.3 p-y parameters for the A1466 Bridge

Table 3.3 and 3.4 present the parameters of the p-y curves for Bridge A1466, specifically addressing clay layers and sand layers, excluding liquefaction and group pile effects, respectively. The effects of liquefaction and pile groups were subsequently considered.

According to equation (2.4),  $(r_u)$  is the pore pressure ratio,  $(p')$  is the average mean effective stress, and  $(p'_c)$  is derived from the specified solid soil parameters. The impact of liquefaction on soil-pile interaction is influenced by strain history, strain rate, soil type, and soil density. To

account for these factors, the PyLiq1 material model was used to define the soil springs materials in the sand layers in Bridge A1466. The input ground motion updated the excess pore water pressure, and the p-y curve model was adjusted at each time step. The soil was modeled using Four Node Quad elements with the Fluid Solid Porous material model in OpenSees.

$$r_u = 1 - \frac{p'}{p_c} \quad (3.4)$$

Table 3.3 p-y model parameters of the clay layers at the A1466 Bridge site (Chen et al. 2005)

Spring location	Spring No.	z' (m)	Clay type	y <sub>50</sub> (mm)	P <sub>ult</sub> (kN/m)	z <sub>cr</sub> (m)
Abutments	1	2.9	medium	8.23	74.9	12.1
	2	4.12	medium	8.23	172.5	13.76
	3	5.34	medium	8.23	201	14.01
	4	6.56	medium	8.23	201	14.01
	5	7.78	medium	8.23	305.8	14.63
	6	9	medium	8.23	305.8	14.63
	7	10.22	soft	16.15	26.2	7.73
Bents	1	1.83	medium	8.23	76.7	3.2
	2	3.05	medium	8.23	99.4	3.86
	3	4.27	soft	16.15	21.8	2.14
	4	5.49	medium	8.23	107.5	3.86
	5	6.71	medium	8.23	107.5	3.86

Table 3.4 p-y model parameters of the sand layers at the A1466 bridge site (Chen et al. 2005)

location	Spring No.	z' (m)	Sand type	ki (kN/m)
Abutments	8	11.44	medium	227200
	9	12.66	medium	251400
	10	13.88	medium	275700
	11	15.1	medium	299900
	12	16.32	medium	324100
	13	17.54	medium	348400
	14	18.76	medium	372600
	15	19.98	medium	396800
Bents	6	7.93	loose	52500
	7	9.15	medium	181700
	8	10.37	medium	206000
	9	11.59	medium	230200
	10	12.81	Dense	530100

Pile groups do not resist lateral loading as efficiently as single piles due to the overlapping of soil stress within the pile group. To address this, p-multipliers were used to reduce the p-y maximum capacity, thereby reflecting the group pile effect. An analysis of  $2 \times 2$  and  $3 \times 3$  pile group shake table tests conducted at the University of California-Berkeley/PEER Center Earthquake Simulator Laboratory revealed that the p-multipliers are primarily related to the peak ground acceleration of the input motion. Figure 3.9 illustrates the results for different footing classifications.

For Bridge A1466, which consists of a pile group with eight piles, the effect of p-multipliers was taken as a weighted average according to the direction of the maximum peak ground acceleration during an earthquake. A logical methodology was employed. Figure 3.10 depicts the configuration of the eight-pile group. It was hypothesized that the fault-parallel component of motion (along the longitudinal axis) would cause deformation in the six outer piles similar to a  $3 \times 3$  pile group, while the two inner piles would deform similarly to a  $2 \times 2$  pile



group. Conversely, for the fault-normal component of motion (along the transverse axis), the six outer piles were expected to deform like a  $2 \times 2$  pile group, and the two inner piles were anticipated to deform as part of a  $3 \times 3$  pile group, which represents the lower bound.

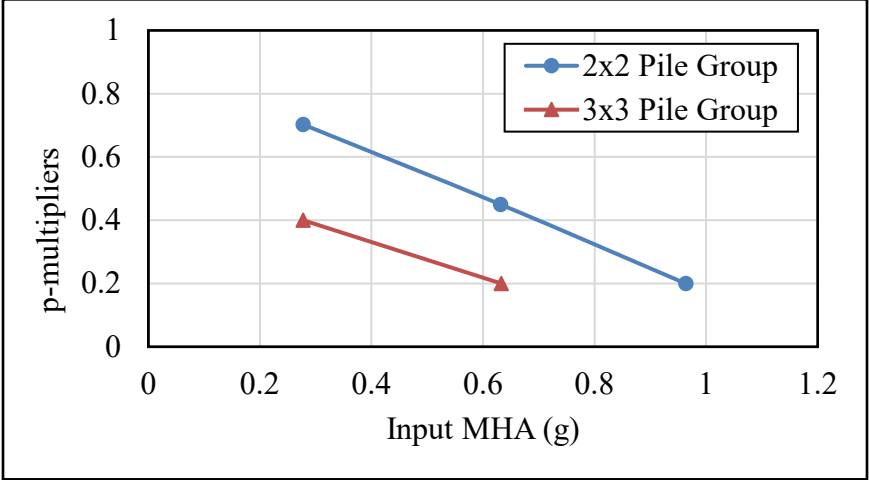


Figure 3.9 p-multipliers with maximum horizontal acceleration relationship

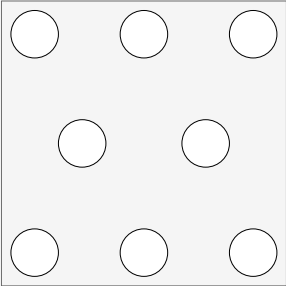


Figure 3.10 8-piles group configuration in bridge A1466

3.1.3.4  $\tau$ -z curves model

The TzSimple1 material model was employed in this study. The nonlinear  $\tau$ -z behavior comprises elastic and plastic components, with a damping dashpot connected to the elastic component that relates to the velocity. Equation (3.5) describes the plastic component of the

model, while equation (3.6) describes the elastic component of the model, where:  $t$  is the shear force on the pile per unit length,  $t_p$  is the plastic shear component,  $t_e$  is the elastic shear component,  $c$  is a constant,  $z_0$  is the vertical displacement at the start of the current plastic cycle,  $z_{50}$  is the displacement at which 50% of  $t_{ult}$  is mobilized during monotonic loading, and  $C_e$  is a constant that defines the normalized elastic stiffness. Figure 3.11 shows the  $\tau$ - $z$  model used in this study.

$$t^p = t_{ult} - (t_{ult} - t_o^p) \left[ \frac{cz_{50}}{cz_{50} + |z_p - z_o^p|} \right]. \quad (3.5)$$

$$t^e = C_e \frac{t_{ult}}{z_{50}} z^e. \quad (3.6)$$

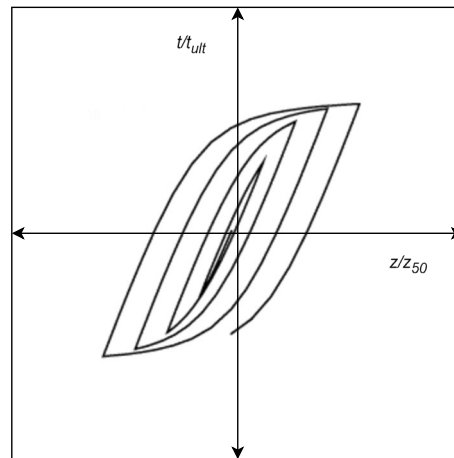


Figure 3.11 TzSimple1 Material used in this study

### 3.1.3.5 $\tau$ - $z$ parameters for the L472 Bridge

The parameters of the soil springs in various bents of the L472 bridge are detailed in Table 3.5. The shear capacity was calculated by multiplying the shear stress by the perimeter of

the pile and then by the tributary length, adjusted for the elevation difference between the springs.

Table 3.5  $\tau$ - $z$  parameters of the soil springs at the L472 Bridge site (Chen et al. 2005)

<b>Bent No.</b>	<b>Spring No.</b>	<b><math>z'</math> (m)</b>	<b><math>k_i</math> (kN/m)</b>	<b><math>\tau_f</math> (kN)</b>	<b><math>z_{50}</math> (mm)</b>
1 and 6	1	6.64	29400	80.7	1.372
	2	7.64	115100	56.7	0.246
	3	8.64	120500	62.1	0.258
	4	9.64	126100	82.6	0.328
	5	10.64	131600	89.9	0.342
	6	11.64	136800	97.1	0.355
	7	12.64	141800	104.4	0.368
	8	13.64	146600	111.7	0.381
	9	14.64	151300	118.9	0.393
2 and 5	1	4.15	29400	52.4	0.891
	2	4.65	77800	31.5	0.202
	3	5.65	86300	38.7	0.224
	4	6.65	94100	46	0.244
	5	7.65	101200	53.2	0.263
	6	8.65	107900	60.5	0.280
	7	9.65	114200	67.7	0.296
	8	10.65	120200	75	0.312
	9	11.65	125900	82.3	0.327
	10	12.65	131300	89.5	0.341
3 and 4	1	3.44	67600	23.8	0.176
	2	4.44	77300	31	0.201
	3	5.44	85800	38.3	0.223
	4	6.44	93600	45.5	0.243
	5	7.44	100800	52.8	0.262
	6	8.44	107500	60	0.279
	7	9.44	113800	67.3	0.296
	8	10.44	119800	74.6	0.311
	9	11.44	125500	81.8	0.326

### 3.1.3.6 $\tau$ - $z$ parameters for the A1466 Bridge

The parameters of the soil springs in the bents and abutments of the A1466 bridge are detailed in Table 3.6. The shear capacity was calculated by multiplying the shear stress by the

perimeter of the pile and then by the tributary length, accommodated for the elevation difference between the springs.

Table 3.6  $\tau$ -z parameters of the soil springs at the A1466 Bridge site (Chen et al. 2005)

Location	Spring No.	$z'$ (m)	$\tau$ (kPa)	$k_i$ (kN/m)	$\tau_{ult}$ (kN)	$z_{50}$ (mm)
Abutments	1	2.9	39.7	13000	46.4	1.785
	2	4.12	70.3	26900	82.1	1.526
	3	5.34	84.1	31100	98.2	1.579
	4	6.56	90.8	31200	106.1	1.700
	5	7.78	126.1	47900	147.3	1.538
	6	9	132.8	48000	155.1	1.616
	7	10.22	62.8	4000	73.4	9.175
	8	11.44	62.9	60300	73.5	0.609
	9	12.66	70.2	64100	82	0.640
	10	13.88	77.5	67600	90.5	0.669
	11	15.1	84.8	71000	99.1	0.698
	12	16.32	92.1	74200	107.6	0.725
	13	17.54	99.4	77200	116.1	0.752
	14	18.76	106.7	80200	124.6	0.777
	15	19.98	114	83000	133.2	0.802
Bents	1	1.83	49.4	155200	461.7	1.487
	2	3.05	56	156300	523.4	1.674
	3	4.27	39.2	31000	366.4	5.910
	4	5.49	69.3	158000	647.7	2.050
	5	6.71	75.9	158600	709.3	2.236
	6	7.93	53.8	518000	502.8	0.485
	7	9.15	61.1	555800	571	0.514
	8	10.37	68.4	591100	639.3	0.541
	9	11.59	75.7	624700	707.5	0.566
	10	12.81	83	656100	775.7	0.591

### 3.1.3.7 q-z curves model and parameters for the two bridges

The q-z behavior is comprised of three components: elastic, plastic, and gap. The gap component consists of a bilinear closure spring in parallel with a nonlinear drag spring. The plastic component is represented in equation (3.7), while the nonlinear drag component is depicted in equation (3.8). In these equations  $q_{ult}$  represents the ultimate capacity of the q-z

material,  $z_{50}$  is the vertical displacement at which 50% of  $q_{ult}$  is mobilized in monotonic loading,  $z^p$  is the plastic component of the displacement, and  $z^g$  is the gap component of the displacement.

$$q = q_{ult} - (q_{ult} - q_o) \left[ \frac{cz_{50}}{cz_{50} + |z_p - z_o^p|} \right]. \quad (3.7)$$

$$q^d = C_d q_{ult} - (C_d q_{ult} - q_o^d) \left[ \frac{z_{50}}{z_{50} + 2|z^g - z_o^g|} \right]. \quad (3.8)$$

Table 3.7 presents the detailed parameters used to model the q-z soil springs in the two bridges. One spring on each pile was defined at the tip of the pile. The stress was multiplied by the tributary area, which is the cross-sectional area of the piles. The area of the piles used in bridge L472 was 0.132 m<sup>2</sup> (201.06 sq.in.), while the area of the piles used in bridge A1466 was 0.073 m<sup>2</sup> (113.1 sq.in.).

Table 3.7 q-z parameters for (L472 and A1466) bridges (Chen et al. 2005)

Bridge	location	G <sub>i</sub> (kPa)	Q <sub>f</sub> (kN)
L472	1 & 6	151300	857.6
	2 & 5	131300	638.7
	3 & 4	125500	584
A1466	Abutment	163200	971.9
	Bents	139300	708.3

### 3.1.3.8 Radiation dampers in the foundation model

The dampers were modeled in each orthogonal direction to simulate the energy loss caused by the interaction between the soil and the foundation. Equation (3.9) depicts the damping effect, where  $C$  represents the radiation damping (kN-sec/m),  $\rho$  is the density of the soil (kN/m<sup>3</sup>),  $V_s$  is the shear wave velocity (m/sec), and  $D$  is the pile diameter (m). In the model, each soil spring material model (p-y,  $\tau$ -z, and q-z) was defined with a viscous damping property. The parameters of the damping properties for the two bridges are shown in Table 3.8.

$$C = 2D\rho V_s \left[ 1 + \frac{3.4}{\pi(1-\nu)} \right]. \quad (3.9)$$

Table 3.8 Damping coefficients used in the bridge models (Chen et al. 2005)

Bridge	L472		A1466	
location	Bents (1-2), (5-6)	Bents (3-4)	Abutments	Bents
Spring No.	c (kN-sec/m)	c (kN-sec/m)	c (kN-sec/m)	c (kN-sec/m)
1	546.7	567.9	391.7	461.8
2	546.7	567.9	554	461.8
3	567.9	697.4	594.1	573.5
4	567.9	697.4	594.1	573.5
5	697.4	762.9	732.9	573.5
6	697.4	762.9	732.9	573.5
7	762.9	869.7	214.6	573.5
8	762.9	869.7	965.5	573.5
9	869.7	869.7	992.4	754.6
10	869.7	-	1017.2	754.6
11	-	-	1040.4	-
12	-	-	1062.1	-
13	-	-	1082.5	-
14	-	-	1101.9	-
15	-	-	1120.3	-

### 3.2 Nonlinear static pushover analysis

A nonlinear static pushover analysis was conducted on the two bridges to evaluate their maximum drifts and base shear, allowing for a comparison of their ductility and plastic ranges.

Figure 3.12 presents the results of the displacement-controlled pushover analysis.

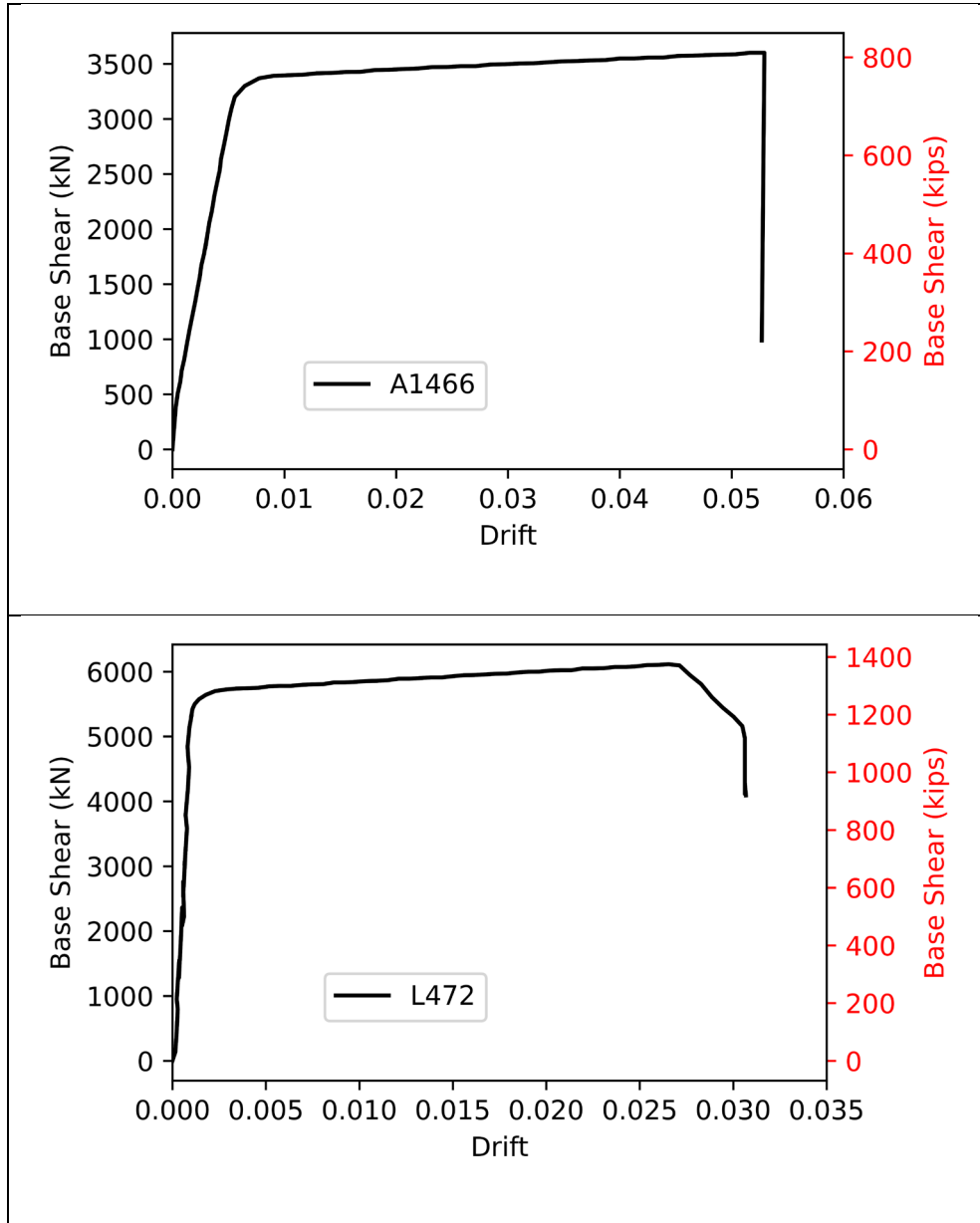


Figure 3.12 Nonlinear static pushover analysis for (A1466 and L472) bridges

The analysis indicates that the maximum base shear for bridge L472 was higher than that for bridge A1466 due to the greater number of columns in L472. However, the columns in bridge A1466 exhibited higher ductility, with a maximum drift of 0.053 compared to 0.031 in bridge L472. This enhanced ductility is attributed to the circular columns in bridge A1466, which offer better confinement than the square columns in bridge L472, resulting in an overall superior ductile performance.

### 3.3 Dynamic characteristics of the L472 and A1466 bridges

The first four vibration modes of each of the two bridges are presented in Table 3.9. results shows that the A1466 bridge was more flexible, with a fundamental period of  $T_0=1.91$  seconds compared to 0.709 seconds for the L472 bridge. This increased flexibility in the A1466 bridge was attributed to its longer spans and the presence of only one fixed bearing for the deck in the road direction.

Table 3.9 Vibration Modes periods of (A1466 and L472) bridges

<b>Bridge No.</b>	<b>A1466</b>	<b>L472</b>
<b>Mode #</b>	<b>Period (sec)</b>	<b>Period (sec)</b>
1	1.908	0.709
2	0.428	0.547
3	0.406	0.503
4	0.351	0.452



### 3.4 Nonlinear time history analysis

The ground motion records were utilized as inputs for the Nonlinear Time History Analysis (NLTHA) of the two bridges. The analysis employed different algorithms at each time step to ensure convergence, specifically Newton, Modified Newton, and Newton with Line Search algorithms. These algorithms were implemented to maintain convergence within acceptable limits.

The analysis utilized the “SuperLU” SOE system, a well-established and widely used library renowned for its robustness, efficiency, and scalability on parallel computing platforms. The model employed the Reverse Cuthill-McKee (RCM) numbering algorithm, a graph renumbering technique designed to reduce the bandwidth of the system matrices. This reduction can lead to significant computational savings during the solution process and can greatly enhance the performance of direct solvers such as the “SuperLU” solver by minimizing the fill-in (non-zero entries) in the factorized matrices.

Convergence of the solution was evaluated using the “NormDispIncr” convergence test, which is based on the norm of the incremental displacement vector between successive iterations. This test verifies if the norm of the incremental displacement vector is smaller than a specified tolerance value, indicating that the solution has converged within the desired accuracy.

The NLTHA was conducted using Rayleigh damping for the entire model and the Newmark integrator method. The analysis was performed for the 20,930 ground motion records.

## Chapter 4 Data Processing

### 4.1 Damage indices and classification.

According to HAZUS the damage states of RC bridges are classified, HAZUS defines four damage states based on the extent of damage to the bridge structures during seismic event as shown in Table 4.4

Table 4.1 Definition of the limit states according to HAZUS (Emergency Management Agency 2022)

<b>Damage State</b>	<b>Definition</b>
Slight/minor	minor cracking and spalling to the abutment, cracks in shear keys at abutments, minor spalling and cracks at hinges, minor spalling at the column (damage requires no more than cosmetic repair) or minor cracking to the deck.
Moderate	column experiencing moderate (shear cracks) cracking and spalling (column structurally still sound), moderate movement of the abutment (<2"), extensive cracking and spalling of shear keys, any connection having cracked shear keys or bent bolts, keeper bar failure without unseating, rocker bearing failure or moderate settlement of the approach.
Extensive/severe	column degrading without collapse – shear failure - (column structurally unsafe), significant residual movement at connections, or major settlement approach, vertical offset of the abutment, differential settlement at connections, shear key failure at abutments.
Complete	column collapsing and connection losing all bearing support, which may lead to imminent deck collapse, tilting of substructure due to foundation failure.

To quantify the damage states and compute the damage state for each NLTHA model (Y. Park and Ang 1985) proposed a damage index that was later modified by (Kunnath et al. 1992) is given in equation (4.1)

$$DI = \frac{\phi_m - \phi_y}{\phi_u - \phi_y} + \frac{\beta}{M_y \phi_u} E_T \quad (4.1)$$

Such that  $\phi_m$  is the maximum curvature in the beam or column during the time history analysis,  $\phi_y$  is the yielding curvature,  $\phi_u$  is the ultimate curvature,  $E_T$  is the dissipated hysteretic energy,  $M_y$  is the yielding moment of the cross-section, and  $\beta$  is a dimensionless constant, typically set to 0.5 and used to account for the contribution of cyclic loading to structural damage in this study. This local damage index has been widely employed in the literature for the inelastic assessment of structures. Additionally, this damage index is used to determine an overall structural damage index (OSDI), which is computed as a weighted average of the local damage indices. The weights are based on the energy dissipated at each cross section or element, as shown in equation (4.2), OSDI can be determined for the entire structure.

$$OSDI = \sum_{i=1}^n DI_i \left( \frac{E_{Ti}}{\sum_{i=1}^n E_{Ti}} \right) \quad (4.2)$$

Where  $n$  is the total number of elements or cross-sections,  $DI_i$  is the damage index for the  $i^{th}$  cross-section and element,  $E_{Ti}$  is the energy dissipated of the  $i^{th}$  cross-section or element. Y. J. Park, Ang, and Wen (1987) proposed a detailed classification, presented in Table 4.2, which correlates the damage index with the damage state of the structure.

Table 4.2 Correlation between damage indices and damage classifications

<b>DI or OSDI</b>	<b>Degree of damage</b>	<b>State of building</b>
<0.10	Slight	Slight damage
0.10-0.25	Minor	Minor damage
0.25-0.40	Moderate	Repairable
0.40-1.0	Severe	Beyond repair
>1.0	Collapse	Loss of building

The damage indices for the 20,930 models were computed and classified into five groups: none, slight, moderate, extensive, and collapse. The classification of the collapse stage was performed using two different approaches: *Approach (A)*: Any model with a drift ratio higher than 12% was removed from the collapse range, based on the results of the pushover analysis. This was done because such high drift ratios are considered unrealistic. *Approach (B)*: The analysis was stopped after a 20% loss and degradation in stiffness, assuming the bridge had collapsed at this point. This approach ensures that the drift ratios remain realistic and includes a higher number of models in the classification training. The classification results were: None: 3,183 models, Minor: 4,132 models, Moderate: 4,402 models, Severe: 6,164 models, Collapses using approach (A): 788 models, And Collapses using approach (B): 3,049 models.

To ensure better performance of the trained artificial neural network models for the ground motion classifier, balanced datasets were used. In Approach A, 788 randomly selected records from each class resulted in a total of 3,940 records. In Approach B, 3,049 randomly selected records from each class resulted in a total of 15,245 ground motion records. This balancing of the datasets leads to improved training performance.

#### 4.2 Intensity measures

Intensity measures (IMs) are parameters used to quantify the severity or intensity of ground motions during an earthquake (IMs) are scalar or vector quantities derived from the

recorded ground motion time histories, such as acceleration, velocity, or displacement time series. They aim to capture the characteristics of the ground motion that are most relevant to the structural response and potential for damage.

In fragility analysis, intensity measures (IMs) are used to estimate the probability that an engineering demand parameter (D) will exceed the structural capacity (C) through an approximated fragility probability function  $p[D > C|IM]$ . The precision of this function relies heavily on the chosen IMs and how well they reflect the ground motion's characteristics and intensity. Traditional approaches typically employ a single IM to create a smooth fragility curve using the cloud method. The cloud method models the seismic demand with a lognormal correlation to the IM, expressed in equations (4.3) and (4.4).

$$\hat{D} = a(IM^b). \quad (4.3)$$

$$\ln(\hat{D}) = b \cdot \ln(IM) + \ln(a). \quad (4.4)$$

In equation (2.10)  $\hat{D}$  represents the median estimate of the engineering demands based on a single IM, with  $a$  and  $b$  being regression constants. The assumption is that D is logarithmically related to the IM and normally distributed around the median  $\ln(\hat{D})$ . The standard deviation of this distribution is shown in equation (4.5)

$$\beta_{D|IM} \cong \sqrt{\frac{\sum(\ln(d_i) - \ln(aIM^b))^2}{N - 2}}. \quad (4.5)$$

Here,  $D_i$  and  $IM_i$  are the demand and IM for the  $i - th$  ground motion record, and  $N$  is the total number of records. The probability function used to estimate the likelihood of  $D$  exceeding  $C$  is described in equation (4.6), utilizing the normal distribution function  $\Phi$ .

$$p(D \geq d|IM) = 1 - \Phi \left[ \frac{\ln d - \ln(aIM^b)}{\beta_{D|IM}} \right]. \quad (4.6)$$

Furthermore, the probability of  $D$  exceeding  $C$  at a specific IM level fragility estimate is shown in equation (x) Such that  $\beta_c$  is the lognormal standard deviation of  $C$ .

$$p(D \geq C|IM) = \Phi \left[ \frac{\ln(\hat{D}/\hat{C})}{\sqrt{\beta_{D|IM}^2 + \beta_c^2}} \right]. \quad (4.7)$$

Fragility analysis traditionally relies on a single intensity measure (IM), leading to significant uncertainty in results, which complicates earthquake loss estimation and response decision-making. To address this uncertainty and provide a more precise method for classifying infrastructure damage, particularly for bridges, this study employed multivariate artificial neural network (ANN) seismic classification.

The classification model categorized the damage into five levels: none, minor, moderate, severe, and collapse, based on multiple IMs.

For the analysis, IMs from 20,930 ground motion records were calculated and used as inputs for the classification models. Considering that bridges are longitudinal structures with significantly different stiffness in the longitudinal, transverse, and vertical directions, the study

accounted for this directional complexity. Unlike more symmetrical structures like buildings, bridges require directional-specific IM calculations.

To manage this complexity, IMs were calculated for different directions. For instance, peak ground acceleration (PGA) was used as a parameter and calculated for the X (longitudinal), Y (transverse), and Z (vertical) components. This approach enabled the ANN model to differentiate between two ground motions with the same resultant IMs but in different directions.

Table 4.3 provides the IMs used in this study, along with equations and definitions, Table 4.4 provides the maximum and minimum of the IMs and their corresponding components in X, Y and Z directions.

Table 4.3 Definitions and equations of the IMs used in this study

<i>IMs</i>	<i>Equation</i>	<i>Definition</i>
<i>PGA</i>	$\max \ddot{u}_g(t) $ (4.8)	Peak ground acceleration
<i>ASQ</i>	$\int_0^{t_{tot}} [\ddot{u}_g(t)]^2 dt$ (4.9)	Squared acceleration, where $t_{tot}$ is the total duration of a record.
<i>ARS</i>	$\sqrt{\int_0^{t_{tot}} [\ddot{u}_g(t)]^2 dt}$ (4.10)	Square root of ASQ.
<i>Ia</i>	$\frac{\pi}{2g} \int_0^{t_{tot}} [\ddot{u}_g(t)]^2 dt$ (4.11)	Arias intensity, where $g$ is the gravitational acceleration.
<i>Arms</i>	$\sqrt{\frac{1}{t_{tot}} \int_0^{t_{tot}} [\ddot{u}_g(t)]^2 dt}$ (4.12)	Root-mean-square acceleration.

<i>IMs</i>	<i>Equation</i>		<i>Definition</i>
<i>Ic</i>	$Arms^{1.5} \cdot t_2^{0.5}$	(4.13)	Characteristic intensity, where $t_2$ is a duration-related IM below.
<i>EPA</i>	$\frac{1}{2.5} \int_{0.1}^{2.5} S_a(T, 0.05) dT$	(4.14)	Effective peak acceleration from Sa
<i>SaTf1</i>	$S_a(T_1, 0.05)$	(4.15)	Spectral acceleration Sa at fundamental period $T_1$ of a structure with 5% damping.
<i>SaTf2</i>	$S_a(T_2, 0.05)$	(4.16)	Spectral acceleration Sa at second period $T_2$
<i>SaTf3</i>	$S_a(T_3, 0.05)$	(4.17)	Spectral acceleration Sa at third period $T_3$
<i>SaTf4</i>	$S_a(T_4, 0.05)$	(4.18)	Spectral acceleration Sa at fourth period $T_4$
<i>Sa-0.3</i>	$S_a(T = 0.3, 0.05)$	(4.19)	Spectral acceleration $S_a$ at 0.3 s
<i>Sa-1.0</i>	$S_a(T = 1.0, 0.05)$	(4.20)	Spectral acceleration $S_a$ at 1.0 s
<i>Sa-3.0</i>	$S_a(T = 3.0, 0.05)$	(4.21)	Spectral acceleration $S_a$ at 3.0 s
<i>CSA</i>	$S_a(T_1, 0.05) \left( \frac{S_a(2T_1, 0.05)}{S_a(T_1, 0.05)} \right)^{0.5}$	(4.22)	Cordova spectral acceleration.
<i>ASI</i>	$\int_{0.1}^{0.5} S_a(T, 0.05) dT$	(4.23)	Acceleration spectral intensity.



<i>IMs</i>	<i>Equation</i>		<i>Definition</i>
<i>CAV</i>	$\int_0^{t_{tot}}  \ddot{u}_g(t)  dt$	(4.24)	Cumulative absolute velocity.
<i>PGV</i>	$\max  \dot{u}_g(t) $	(4.25)	Peak ground velocity.
<i>VSQ</i>	$\int_0^{t_{tot}} [\dot{u}_g(t)]^2 dt$	(4.26)	Squared velocity.
<i>VRS</i>	$\sqrt{\int_0^{t_{tot}} [\dot{u}_g(t)]^2 dt}$	(4.27)	Root-square velocity of <i>VSQ</i> .
<i>Vrms</i>	$\sqrt{\frac{1}{t_{tot}} \int_0^{t_{tot}} [\dot{u}_g(t)]^2 dt}$	(4.28)	Root-mean-square velocity.
<i>Ih</i>	$\int_{0.1}^{2.5} S_v(T, 0.05) dT$	(4.29)	Intensity of pseudo-velocity spectrum $S_v$
<i>CAD</i>	$\int_0^{t_{tot}}  \ddot{u}_g(t)  dt$	(4.30)	Cumulative absolute displacement.
<i>EPV</i>	$\frac{1}{2.5} \int_{0.1}^{2.5} S_v(T, 0.05) dT$	(4.31)	Effective peak velocity from $S_v$
<i>SvTf1</i>	$S_v(T_1, 0.05)$	(4.32)	$S_v$ at the fundamental period $T_1$ of a structure with 5% damping.
<i>SvTf2</i>	$S_v(T_2, 0.05)$	(4.33)	$S_v$ at the second period $T_2$
<i>SvTf3</i>	$S_v(T_3, 0.05)$	(4.34)	$S_v$ at the third period $T_3$

<i>IMs</i>	<i>Equation</i>		<i>Definition</i>
<i>SvTf4</i>	$S_v(T_4, 0.05)$	(4.35)	$S_v$ at the fourth period $T_4$
<i>VC1</i>	$PGV \cdot t_2^{0.25}$	(4.36)	A compound index of $PGV$ and $t_2$ .
<i>VC2</i>	$(PGV)^{\frac{2}{3}} \cdot t_2^{\frac{1}{3}}$	(4.37)	A compound index of $PGV$ and $t_2$ .
<i>PGD</i>	$\max u_g(t) $	(4.38)	Peak ground displacement.
<i>DSQ</i>	$\int_0^{t_{tot}} [u_g(t)]^2 dt$	(4.39)	Squared displacement.
<i>DRS</i>	$\sqrt{\int_0^{t_{tot}} [u_g(t)]^2 dt}$	(4.40)	Root-square displacement of $DSQ$ .
<i>Drms</i>	$\sqrt{\frac{1}{t_{tot}} \int_0^{t_{tot}} [u_g(t)]^2 dt}$	(4.41)	Root-mean-square displacement
<i>CAI</i>	$\int_0^{t_{tot}}  u_g(t)  dt$	(4.42)	Cumulative absolute intensity.
<i>EPD</i>	$\frac{1}{2.5} \int_{0.1}^{2.5} S_d(T, 0.05) dT$	(4.43)	Effective peak displacement from $S_d$
<i>SdTf1</i>	$S_d(T_1, 0.05)$	(4.44)	$S_d$ at the fundamental period $T_1$ of a structure with 5% damping
<i>SdTf2</i>	$S_d(T_2, 0.05)$	(4.45)	$S_d$ at the second period $T_2$

<i>IMs</i>	<i>Equation</i>		<i>Definition</i>
<i>SdTf3</i>	$S_d(T_3, 0.05)$	(4.46)	$S_d$ at the third period $T_3$
<i>SdTf4</i>	$S_d(T_4, 0.05)$	(4.47)	$S_d$ at the fourth period $T_4$
<i>DC</i>	$(PGD)t_2^{\frac{1}{3}}$	(4.48)	A compound index of <i>PGD</i> and $t_2$ .
$t_1$	$t(0.75Ia) - t(0.05Ia)$	(4.49)	Time duration between 75% <i>Ia</i> and 5% <i>Ia</i> .
$t_2$	$t(0.95Ia) - t(0.05Ia)$	(4.50)	Time duration between 95% <i>Ia</i> and 5% <i>Ia</i> .
$t_3$	$t_l(a > 0.02g) - t_f(a > 0.02g)$	(4.51)	The time elapsed between the first and last excursions of acceleration above 0.02 g.
$t_4$	$t_l(a > 0.05g) - t_f(a > 0.05g)$	(4.52)	The time elapsed between the first and last excursions of acceleration above 0.05 g.

Table 4.4 IMs with the maximum and minimum values (resultant, x, y and z) components

<i>IMs</i>	<i>max</i>	<i>min</i>	<i>max (x)</i>	<i>min(x)</i>	<i>max(y)</i>	<i>min(y)</i>	<i>max(z)</i>	<i>min(z)</i>
<i>Arms</i>	30.3	0.026	15.24	0.014	14.59	0.013	28.33	0.008
<i>ARS</i>	141.7	0.156	79.19	0.106	75.83	0.098	104.95	0.061
<i>ASI</i>	14.7	0.010	10.68	0.006	9.83	0.007	8.08	0.004
<i>ASQ</i>	20089.1	0.024	6271	0.011	5750	0.010	11013.78	0.004
<i>CAD</i>	11148.4	3.802	6166	2.609	7472	2.251	2645.66	1.587
<i>CAI</i>	12765.8	0.189	6569	0.080	9380	0.097	2664.91	0.040
<i>CSA</i>	38.4	0.028	29.65	0.016	22	0.021	12.71	0.010

<i>IMs</i>	<i>max</i>	<i>min</i>	<i>max (x)</i>	<i>min(x)</i>	<i>max(y)</i>	<i>min(y)</i>	<i>max(z)</i>	<i>min(z)</i>
<i>DC</i>	1756.3	0.227	-	-	-	-	-	-
<i>Drms</i>	227.2	0.028	155.36	0.014	194.04	0.022	131.31	0.007
<i>DRS</i>	1628.9	0.098	1013	0.047	1325.79	0.070	718.98	0.025
<i>DSQ</i>	2653297	0.010	1027313	0.002	1757722	0.005	516931	0.001
<i>EPA</i>	12.6	0.015	10.61	0.010	9.11	0.011	5.39	0.006
<i>EPD</i>	3133.7	1.912	2373	1.244	1982.97	1.441	2937.23	0.783
<i>EPV</i>	4759.2	3.946	3605	2.544	2986.17	2.978	3137.39	1.535
<i>Ia</i>	3216.7	0.004	1004	0.002	920.84	0.002	1763.55	0.001
<i>Ic</i>	535.1	0.017	145	0.009	136.80	0.008	384.69	0.005
<i>Ih</i>	11898.0	9.866	9014	6.360	7465.42	7.446	7843.47	3.838
<i>PGA</i>	196.3	1.250	145	0.089	124.54	0.061	192.57	0.039
<i>PGD</i>	700.8	0.160	447	0.076	654.96	0.151	491.33	0.059
<i>PGV</i>	1356.0	1.173	1331	0.883	1039.30	1.135	503.21	0.688
<i>Sa-0.3</i>	46.6	0.024	32.24	0.016	33.61	0.018	17.55	0.011
<i>Sa-1.0</i>	18.6	0.008	16.48	0.003	15.79	0.007	3.94	0.002
<i>Sa-3.0</i>	4.8	0.001	4.43	3.35E-04	3.57	0.001	1.88	2.43E-04
<i>SaTf1</i>	43.5	0.025	39.05	0.015	29.32	0.020	19.98	0.009
<i>SaTf2</i>	32.9	0.011	21.86	0.006	25.71	0.009	38.59	0.004
<i>SaTf3</i>	31.4	0.011	21.64	0.006	24.98	0.009	37.28	0.004
<i>SaTf4</i>	25.8	0.011	20.34	0.006	23.96	0.009	35.24	0.004
<i>SdTf1</i>	69.9	0.041	62.71	0.025	47.09	0.032	32.08	0.014
<i>SdTf2</i>	3.5	0.001	2.30	0.001	2.70	0.001	4.05	4.48E-04
<i>SdTf3</i>	3.2	0.001	2.20	0.001	2.54	0.001	3.79	4.36E-04
<i>SdTf4</i>	2.1	0.001	1.64	0.001	1.93	0.001	2.85	3.44E-04
<i>SvTf1</i>	1728.2	1.007	1549	0.613	1163.83	0.798	792.97	0.358
<i>SvTf2</i>	333.5	0.114	221	0.065	260.97	0.094	391.63	0.043
<i>SvTf3</i>	313.3	0.112	216	0.064	249.59	0.092	372.53	0.043
<i>SvTf4</i>	229.3	0.100	181	0.057	213.21	0.082	313.65	0.038
<i>t1</i>	64.6	0.295	63	0.205	67.10	0.370	62.80	0.380
<i>t2</i>	110.9	0.990	111.8	0.845	108.95	1.040	110.63	0.680
<i>t3</i>	77.3	0.395	77.22	0.195	71.52	0.095	59.38	0.135
<i>t4</i>	62.4	0.115	58.7	0.115	51.04	0.250	45.77	0.260
<i>VC1</i>	2295.3	2.770	-	-	-	-	-	-
<i>VC2</i>	247.1	3.484	-	-	-	-	-	-
<i>Vrms</i>	282.6	0.436	219.41	0.245	232.35	0.258	128.19	0.152
<i>VRS</i>	1623.2	2.072	1097.03	1.642	1334.34	1.264	701.91	0.957
<i>VSQ</i>	2634619	4.292	1203476	2.695	1780453	1.597	492682	0.916

In total, 171 parameters were used, representing various IMs and their components. These parameters were normalized to eliminate the effects of unit and scale differences, based on equation (4.53), where  $x_{min}$  and  $x_{max}$  are the minimum and maximum values of each parameter,  $z$  is the normalized value.

$$z = \frac{x - x_{min}}{x_{max} - x_{min}} \quad (4.53)$$

### 4.3 Correlation and ranking of IMs

With 171 intensity measure features, feature ranking and selection are crucial to reducing error and irrelevancy in ANN model formation and enhancing model performance. Using statistical methods, the correlation between the input and target variables will be calculated, ranking the features from most to least correlated. Features with high correlation scores will be considered more important (Hall and Smith 1999).

The correlation between *IMs* and the drift ratios (*DR*) will be evaluated, starting with providing a ranking from most to least important. Riddell (2007) measured the correlation between IMs and various structural responses using the regression fitness  $R^2$  from equation (4.4). Padgett, Nielson, and DesRoches (2008) used indicators like efficiency, which is the standard deviation from equation (4.5), practicality ( $b$  in equation(4.4)) and proficiency in equation (4.54). In summary, IMs with higher  $b$  and  $R^2$ , lower  $\beta_{D|IM}$ , and  $\zeta$  have a higher correlation. These four parameters were calculated between the maximum drift ratio and the intensity measures for all accelerograms, excluding those with unrealistic drift ratios, which were removed during data processing using approach (A).

$$\zeta = \frac{\beta_{D|IM}}{b} \quad (4.54)$$

Table 4.5 displays the correlation parameters of the intensity measures (IM), including  $R^2$ ,  $\beta_{D|IM}$  and  $\zeta$ , for each parameter. As noted earlier, parameters with the highest  $R^2$  and  $b$ , as well as the lowest  $\beta_{D|IM}$  and  $\zeta$ , are deemed the most significant. According to the findings in Table 4.5,  $Ih_y$  and  $EPV_y$  present the highest  $R^2$  and the lowest  $\beta_{D|IM}$  and  $\zeta$ , values. Conversely, VC2 records the highest B parameter. The parameters are ranked in order of importance based on their  $R^2$  scores correlation with maximum drift ratio ( $MDR$ ), from highest to lowest. Figure 4.1 presents a bar plot showing the IMs ranked from highest to lowest  $R^2$ .

Table 4.5 Correlation results of IMs

IM	$R^2$	<b>b</b>	$\beta_{D IM}$	$\xi$	IM	$R^2$	<b>b</b>	$\beta_{D IM}$	$\xi$
<i>Arms</i>	0.790	1.298	0.769	0.593	<i>Sa – 1.0<sub>z</sub></i>	0.612	1.040	1.026	0.987
<i>Arms<sub>x</sub></i>	0.741	1.263	0.838	0.664	<i>Sa – 3.0</i>	0.491	0.784	1.176	1.501
<i>Arms<sub>y</sub></i>	0.819	1.332	0.702	0.527	<i>Sa – 3.0<sub>x</sub></i>	0.462	0.722	1.209	1.675
<i>Arms<sub>z</sub></i>	0.708	1.137	0.888	0.781	<i>Sa – 3.0<sub>y</sub></i>	0.463	0.763	1.208	1.583
<i>ARS</i>	0.790	1.356	0.755	0.557	<i>Sa – 3.0<sub>z</sub></i>	0.379	0.652	1.299	1.992
<i>ARS<sub>x</sub></i>	0.763	1.368	0.802	0.586	<i>SaTf1</i>	0.805	1.305	0.728	0.558
<i>ARS<sub>y</sub></i>	0.838	1.436	0.663	0.462	<i>SaTf1<sub>x</sub></i>	0.788	1.260	0.759	0.602
<i>ARS<sub>z</sub></i>	0.739	1.266	0.841	0.664	<i>SaTf1<sub>y</sub></i>	0.786	1.285	0.763	0.594
<i>ASI</i>	0.833	1.341	0.674	0.503	<i>SaTf1<sub>z</sub></i>	0.744	1.151	0.833	0.724
<i>ASI<sub>x</sub></i>	0.813	1.300	0.713	0.548	<i>SaTf2</i>	0.718	1.157	0.875	0.756
<i>ASI<sub>y</sub></i>	0.831	1.346	0.678	0.504	<i>SaTf2<sub>x</sub></i>	0.698	1.125	0.906	0.805
<i>ASI<sub>z</sub></i>	0.773	1.199	0.785	0.655	<i>SaTf2<sub>y</sub></i>	0.715	1.152	0.880	0.764
<i>ASQ</i>	0.790	0.678	0.755	1.114	<i>SaTf2<sub>z</sub></i>	0.668	0.935	0.950	1.016
<i>ASQ<sub>x</sub></i>	0.763	0.684	0.802	1.172	<i>SaTf3</i>	0.720	1.160	0.873	0.752
<i>ASQ<sub>y</sub></i>	0.838	0.718	0.663	0.924	<i>SaTf3<sub>x</sub></i>	0.699	1.128	0.903	0.801
<i>ASQ<sub>z</sub></i>	0.739	0.633	0.841	1.328	<i>SaTf3<sub>y</sub></i>	0.717	1.155	0.877	0.759
<i>CAD</i>	0.431	0.826	1.243	1.505	<i>SaTf3<sub>z</sub></i>	0.667	0.933	0.951	1.019
<i>CAD<sub>x</sub></i>	0.410	0.805	1.266	1.573	<i>SaTf4</i>	0.731	1.177	0.854	0.726
<i>CAD<sub>y</sub></i>	0.422	0.813	1.253	1.541	<i>SaTf4<sub>x</sub></i>	0.711	1.142	0.887	0.776
<i>CAD<sub>z</sub></i>	0.373	0.835	1.302	1.560	<i>SaTf4<sub>y</sub></i>	0.729	1.174	0.858	0.731
<i>CAI</i>	0.214	0.441	1.461	3.317	<i>SaTf4<sub>z</sub></i>	0.658	0.920	0.963	1.047
<i>CAI<sub>x</sub></i>	0.210	0.427	1.465	3.429	<i>SdTf1</i>	0.805	1.305	0.728	0.558

<b>IM</b>	<b>R<sup>2</sup></b>	<b>b</b>	<b><math>\beta_{D IM}</math></b>	<b><math>\xi</math></b>	<b>IM</b>	<b>R<sup>2</sup></b>	<b>b</b>	<b><math>\beta_{D IM}</math></b>	<b><math>\xi</math></b>
<i>CAI<sub>y</sub></i>	0.190	0.399	1.483	3.717	<i>SdTf1<sub>x</sub></i>	0.788	1.260	0.759	0.602
<i>CAI<sub>z</sub></i>	0.152	0.366	1.515	4.142	<i>SdTf1<sub>y</sub></i>	0.786	1.285	0.763	0.594
<i>CSA</i>	0.852	1.337	0.634	0.474	<i>SdTf1<sub>z</sub></i>	0.744	1.151	0.833	0.724
<i>CSA<sub>x</sub></i>	0.816	1.268	0.708	0.558	<i>SdTf2</i>	0.718	1.157	0.875	0.756
<i>CSA<sub>y</sub></i>	0.851	1.345	0.637	0.473	<i>SdTf2<sub>x</sub></i>	0.698	1.125	0.906	0.805
<i>CSA<sub>z</sub></i>	0.757	1.202	0.813	0.676	<i>SdTf2<sub>y</sub></i>	0.715	1.152	0.880	0.764
<i>DC</i>	0.373	0.679	1.305	1.923	<i>SdTf2<sub>z</sub></i>	0.668	0.935	0.950	1.016
<i>Drms</i>	0.386	0.689	1.292	1.875	<i>SdTf3</i>	0.720	1.160	0.873	0.752
<i>Drms<sub>x</sub></i>	0.382	0.671	1.295	1.931	<i>SdTf3<sub>x</sub></i>	0.699	1.128	0.903	0.801
<i>Drms<sub>y</sub></i>	0.349	0.627	1.329	2.120	<i>SdTf3<sub>y</sub></i>	0.717	1.155	0.877	0.759
<i>Drms<sub>z</sub></i>	0.305	0.600	1.371	2.284	<i>SdTf3<sub>z</sub></i>	0.667	0.933	0.951	1.019
<i>DRS</i>	0.308	0.581	1.370	2.359	<i>SdTf4</i>	0.731	1.177	0.854	0.726
<i>DRS<sub>x</sub></i>	0.307	0.568	1.372	2.416	<i>SdTf4<sub>x</sub></i>	0.711	1.142	0.887	0.776
<i>DRS<sub>y</sub></i>	0.278	0.529	1.400	2.647	<i>SdTf4<sub>y</sub></i>	0.729	1.174	0.858	0.731
<i>DRS<sub>z</sub></i>	0.232	0.493	1.442	2.925	<i>SdTf4<sub>z</sub></i>	0.658	0.920	0.963	1.047
<i>DSQ</i>	0.308	0.291	1.370	4.717	<i>SvTf1</i>	0.805	1.305	0.728	0.558
<i>DSQ<sub>x</sub></i>	0.307	0.284	1.372	4.832	<i>SvTf1<sub>x</sub></i>	0.788	1.260	0.759	0.602
<i>DSQ<sub>y</sub></i>	0.278	0.264	1.400	5.294	<i>SvTf1<sub>y</sub></i>	0.786	1.285	0.763	0.594
<i>DSQ<sub>z</sub></i>	0.232	0.247	1.442	5.849	<i>SvTf1<sub>z</sub></i>	0.744	1.151	0.833	0.724
<i>EPA</i>	0.838	1.330	0.663	0.499	<i>SvTf2</i>	0.718	1.157	0.875	0.756
<i>EPA<sub>x</sub></i>	0.803	1.258	0.731	0.581	<i>SvTf2<sub>x</sub></i>	0.698	1.125	0.906	0.805
<i>EPA<sub>y</sub></i>	0.838	1.348	0.663	0.492	<i>SvTf2<sub>y</sub></i>	0.715	1.152	0.880	0.764
<i>EPA<sub>z</sub></i>	0.758	1.261	0.810	0.643	<i>SvTf2<sub>z</sub></i>	0.668	0.935	0.950	1.016
<i>EPD</i>	0.800	1.313	0.737	0.561	<i>SvTf3</i>	0.720	1.160	0.873	0.752
<i>EPD<sub>x</sub></i>	0.787	1.283	0.760	0.593	<i>SvTf3<sub>x</sub></i>	0.699	1.128	0.903	0.801
<i>EPD<sub>y</sub></i>	0.796	1.315	0.744	0.565	<i>SvTf3<sub>y</sub></i>	0.717	1.155	0.877	0.759
<i>EPD<sub>z</sub></i>	0.761	1.141	0.806	0.707	<i>SvTf3<sub>z</sub></i>	0.667	0.933	0.951	1.019
<i>EPV</i>	0.856	1.383	0.626	0.453	<i>SvTf4</i>	0.731	1.177	0.854	0.726
<i>EPV<sub>x</sub></i>	0.832	1.331	0.676	0.508	<i>SvTf4<sub>x</sub></i>	0.711	1.142	0.887	0.776
<i>EPV<sub>y</sub></i>	0.857	1.398	0.623	0.446	<i>SvTf4<sub>y</sub></i>	0.729	1.174	0.858	0.731
<i>EPV<sub>z</sub></i>	0.782	1.230	0.769	0.625	<i>SvTf4<sub>z</sub></i>	0.658	0.920	0.963	1.047
<i>Ia</i>	0.790	0.678	0.755	1.114	<i>t1</i>	0.053	-0.46	1.604	-3.482
<i>Ia<sub>x</sub></i>	0.763	0.684	0.802	1.172	<i>t1<sub>x</sub></i>	0.054	-0.42	1.603	-3.734
<i>Ia<sub>y</sub></i>	0.838	0.718	0.663	0.924	<i>t1<sub>y</sub></i>	0.076	-0.53	1.584	-2.975
<i>Ia<sub>z</sub></i>	0.739	0.633	0.841	1.328	<i>t1<sub>z</sub></i>	0.102	-0.648	1.559	-2.405
<i>Ic</i>	0.761	0.886	0.805	0.908	<i>t2</i>	0.066	-0.559	1.593	-2.848
<i>Ic<sub>x</sub></i>	0.738	0.899	0.843	0.938	<i>t2<sub>x</sub></i>	0.060	-0.512	1.598	-3.123
<i>Ic<sub>y</sub></i>	0.803	0.942	0.732	0.777	<i>t2<sub>y</sub></i>	0.089	-0.638	1.573	-2.467
<i>Ic<sub>z</sub></i>	0.720	0.845	0.871	1.030	<i>t2<sub>z</sub></i>	0.127	-0.764	1.538	-2.013
<i>Ih</i>	0.856	1.383	0.626	0.453	<i>t3</i>	0.067	0.543	1.591	2.928
<i>Ih<sub>x</sub></i>	0.832	1.331	0.676	0.508	<i>t3<sub>x</sub></i>	0.069	0.470	1.590	3.380
<i>Ih<sub>y</sub></i>	0.857	1.398	0.623	0.446	<i>t3<sub>y</sub></i>	0.064	0.464	1.594	3.434

<b>IM</b>	<b>R<sup>2</sup></b>	<b>b</b>	<b><math>\beta_{D IM}</math></b>	<b><math>\xi</math></b>	<b>IM</b>	<b>R<sup>2</sup></b>	<b>b</b>	<b><math>\beta_{D IM}</math></b>	<b><math>\xi</math></b>
<i>Ih<sub>z</sub></i>	0.782	1.230	0.769	0.625	<i>t3<sub>z</sub></i>	0.006	-0.112	1.640	-14.653
<i>PGA</i>	0.755	1.206	0.815	0.676	<i>t4</i>	0.052	0.346	1.604	4.631
<i>PGA<sub>x</sub></i>	0.730	1.226	0.856	0.698	<i>t4<sub>x</sub></i>	0.049	0.334	1.607	4.818
<i>PGA<sub>y</sub></i>	0.813	1.286	0.713	0.555	<i>t4<sub>y</sub></i>	0.037	0.299	1.617	5.400
<i>PGA<sub>z</sub></i>	0.698	1.049	0.904	0.862	<i>t4<sub>z</sub></i>	0.010	-0.143	1.637	-11.455
<i>PGD</i>	0.474	0.805	1.196	1.486	<i>VC1</i>	0.716	1.183	0.878	0.742
<i>PGD<sub>x</sub></i>	0.458	0.767	1.213	1.581	<i>VC2</i>	0.634	1.649	0.997	0.605
<i>PGD<sub>y</sub></i>	0.435	0.741	1.239	1.672	<i>Vrms</i>	0.685	1.135	0.925	0.815
<i>PGD<sub>z</sub></i>	0.359	0.686	1.318	1.920	<i>Vrms<sub>x</sub></i>	0.657	1.111	0.965	0.868
<i>PGV</i>	0.766	1.206	0.797	0.661	<i>Vrms<sub>y</sub></i>	0.698	1.143	0.905	0.792
<i>PGV<sub>x</sub></i>	0.717	1.163	0.876	0.754	<i>Vrms<sub>z</sub></i>	0.642	1.187	0.984	0.829
<i>PGV<sub>y</sub></i>	0.799	1.227	0.739	0.602	<i>VRS</i>	0.607	1.058	1.033	0.976
<i>PGV<sub>z</sub></i>	0.704	1.259	0.895	0.711	<i>VRS<sub>x</sub></i>	0.582	1.034	1.066	1.030
<i>Sa – 0.3</i>	0.825	1.310	0.689	0.526	<i>VRS<sub>y</sub></i>	0.613	1.056	1.025	0.971
<i>Sa – 0.3<sub>x</sub></i>	0.801	1.264	0.734	0.581	<i>VRS<sub>z</sub></i>	0.552	1.098	1.101	1.003
<i>Sa – 0.3<sub>y</sub></i>	0.809	1.289	0.721	0.559	<i>VSQ</i>	0.607	0.529	1.033	1.953
<i>Sa – 0.3<sub>z</sub></i>	0.729	1.176	0.858	0.729	<i>VSQ<sub>x</sub></i>	0.582	0.517	1.066	2.061
<i>Sa – 1.0</i>	0.706	1.053	0.894	0.848	<i>VSQ<sub>y</sub></i>	0.613	0.528	1.025	1.942
<i>Sa – 1.0<sub>x</sub></i>	0.650	0.968	0.975	1.007	<i>VSQ<sub>z</sub></i>	0.552	0.549	1.101	2.006
<i>Sa – 1.0<sub>y</sub></i>	0.691	1.038	0.916	0.883					



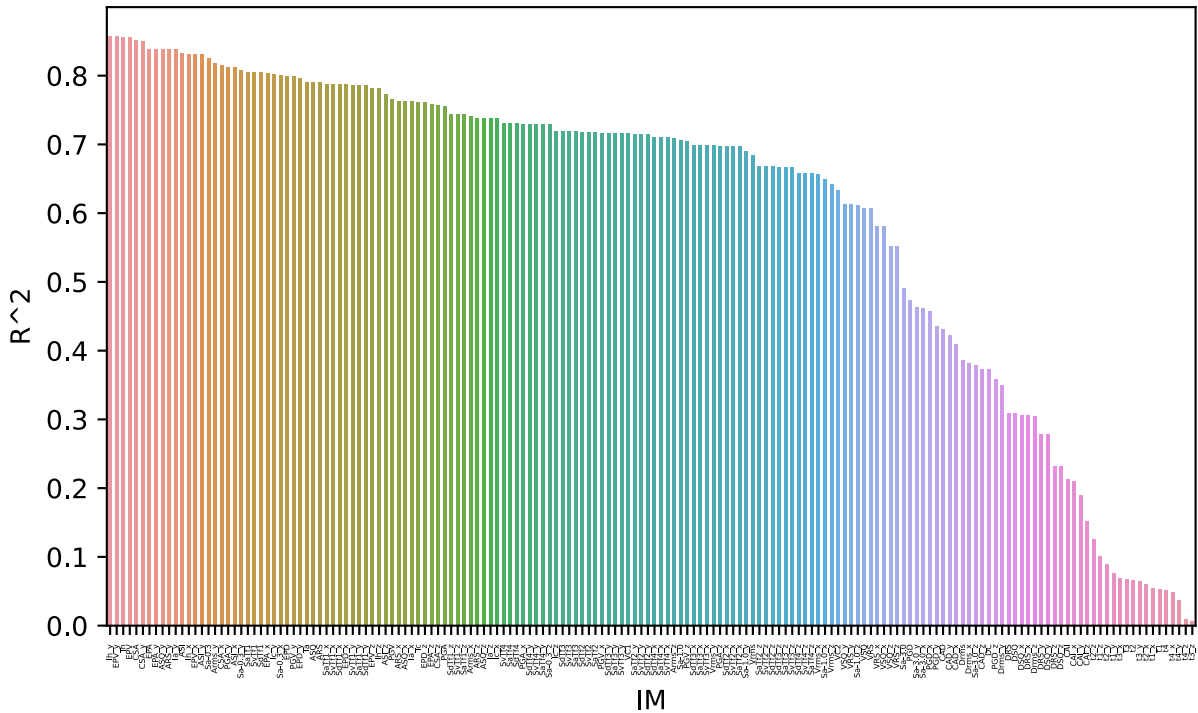


Figure 4.1 Correlation ranking of IMs based on maximum drift ratios

The analysis of IMs ranks the top five crucial features as  $Ih_y$ ,  $EPV_y$ ,  $Ih$ ,  $EPV$  and  $CSA$ . Conversely, the five least important features identified are  $t_4$ ,  $t_{4_x}$ ,  $t_{4_y}$ ,  $t_{4_z}$  and  $t_{3_z}$ . These results align with the findings of Yuan et al. (2022), who similarly observed that  $Ih$  and  $CSA$  were within the most significant IMs in their study on four-story buildings. They also noted that IMs associated with frequencies  $t_1$ ,  $t_2$  and  $t_3$  held less importance.

The most important and useful features were selected as: 1) features with an  $R^2$  value higher than 0.6 were selected and 2) features that demonstrated strong correlation with others. One feature was chosen using the Correlation-based Feature Selection (CFS) algorithm proposed by Hall (2003). This algorithm identifies and eliminates irrelevant, redundant, and noisy features, selecting those that are highly correlated with the target class but uncorrelated with each other. For instance, since  $ARS$  and  $\sqrt{ARS}$  are redundant to each other, only one was chosen. Similarly,

because spectral accelerations are well correlated with spectral velocities and spectral displacements, using spectral accelerations alone was deemed sufficient to mitigate redundancy.

Figure 4.2 depicts a bar plot illustrating the 71 selected IMs chosen according to predefined criteria. These features are deemed most important and will be used for ANN training, ensuring there is no redundancy among them.

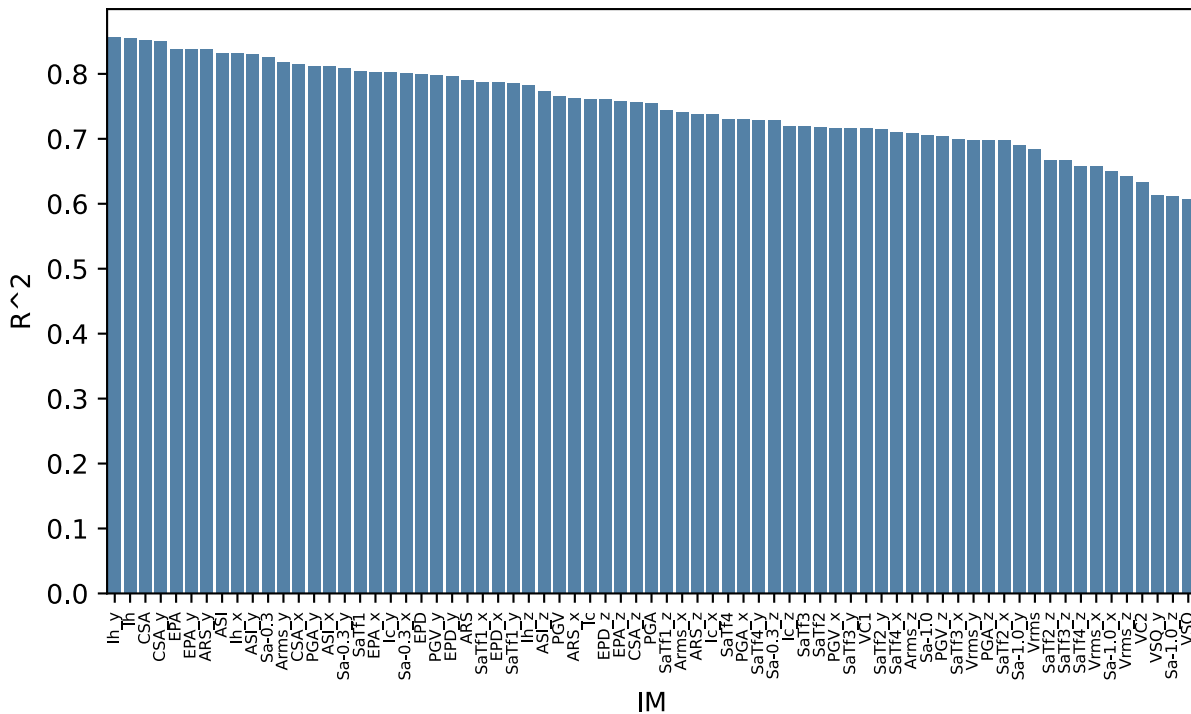


Figure 4.2: Most important IMs ranked based on  $R^2$

The significance of vector-valued IMs is evident in the results, particularly where y-directional IMs show stronger correlations with MDR compared to other values within the same category. This aligns with the orientation of concrete bents in bridges. For instance, Figure 4.3 illustrates the correlation of  $PGA$ ,  $PGA_x$ ,  $PGA_y$ , and  $PGA_z$  with  $MDR$  across 1500 samples of accelerograms, showing  $R^2$  values and standard deviations depicted for each feature.

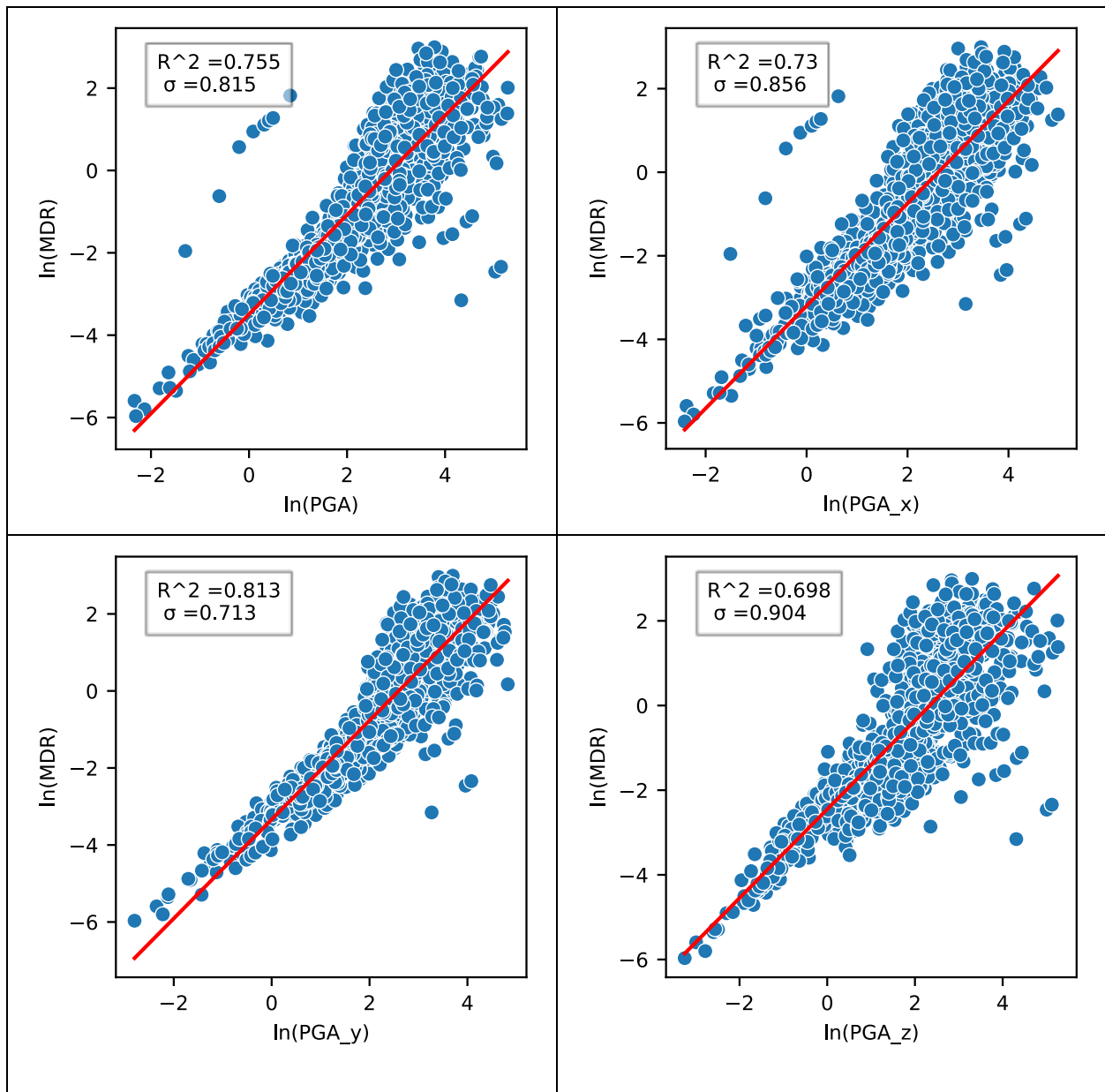


Figure 4.3 Correlation plot between  $PGA$  scalar and directional values with  $MDR$

The analysis reveals that  $PGA_Y$  exhibits the highest  $R^2$  value and the lowest standard deviation, indicating its strong predictive capability and stability. In contrast,  $PGA_X$  and  $PGA_Z$  show lower  $R^2$  values and higher standard deviations.  $PGA$ , as a scalar combining all three directions, falls between these extremes. This underscores the impact of the ground shaking direction on damage calculations for bridges. Utilizing vector-valued IMs can enhance the accuracy of damage prediction and the training of damage classifiers.

Figure 4.4 illustrates correlation plots between spectral accelerations at vibration periods and MDR. It is evident that the highest correlation occurs with spectral accelerations at the fundamental period  $Sa_{Tf1}$ , which corresponds with findings from Yuan et al. (2022).

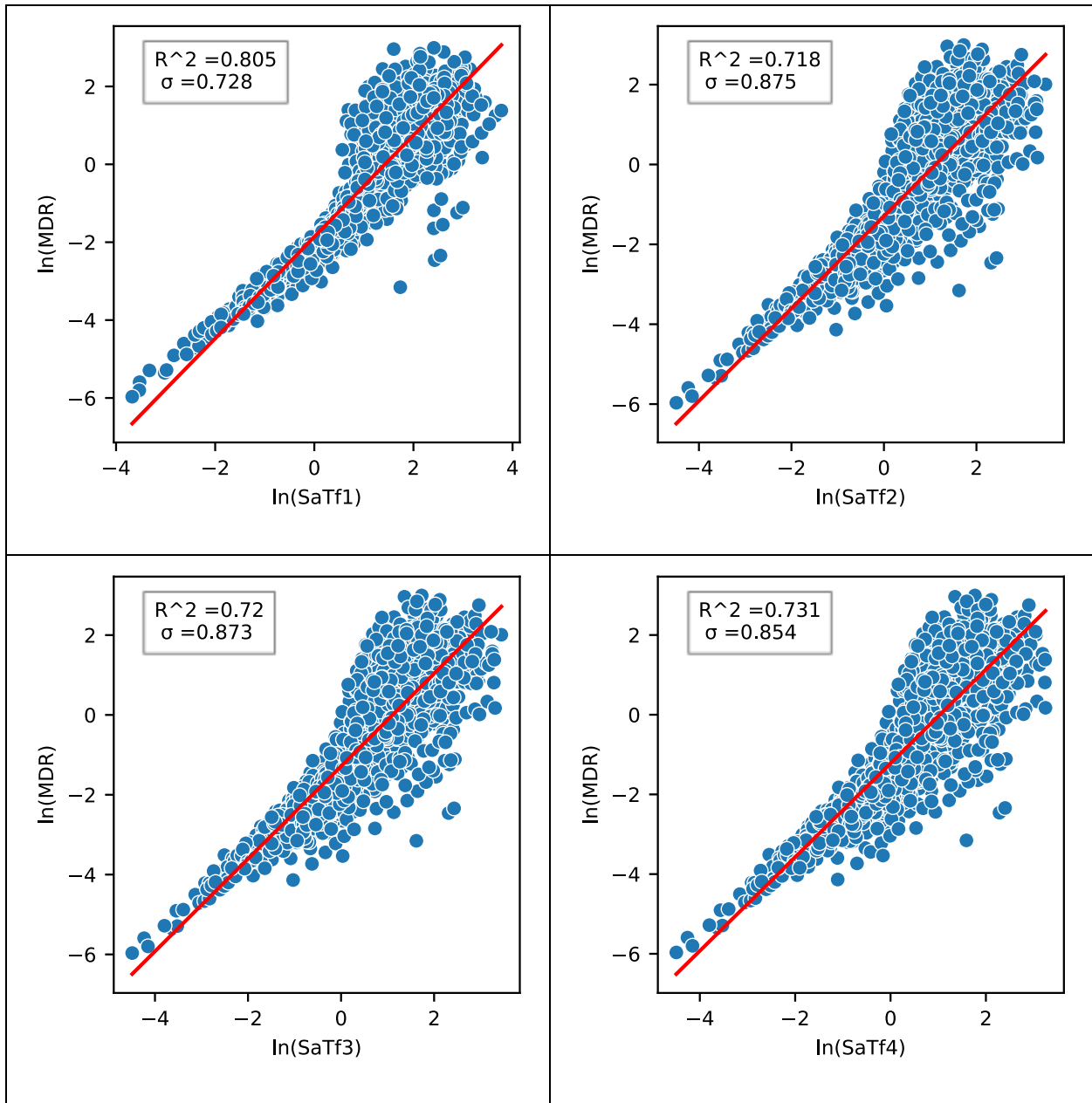


Figure 4.4 Correlation plot between spectral accelerations at vibration periods with *MDR*

5.1 ANN seismic classifier methodology

The classification model was structured with three layers, illustrated in Figure 5.1, the input layer was comprised of 71 of the most significant IMs. Two hidden layers were incorporated, and the output layer represented the damage states derived from NLTHA results. Each layer in the ANN classifier featured fully connected neurons linked by synaptic connections. Synaptic weights were assigned to these connections to form the weight matrices  $W^{L1}$ ,  $W^{L2}$ , and  $W^{L3}$ , the activation functions  $\sigma_1$  and  $\sigma_2$  employed in the two hidden layers were rectified linear units (ReLU), described in equation (5.1), while the activation function  $\sigma_3$  used in the output layer was a SoftMax activation function defined by equation (5.2). (Bridle 1990; Sontag 1992; Haykin 2008; Nair and Hinton 2010).

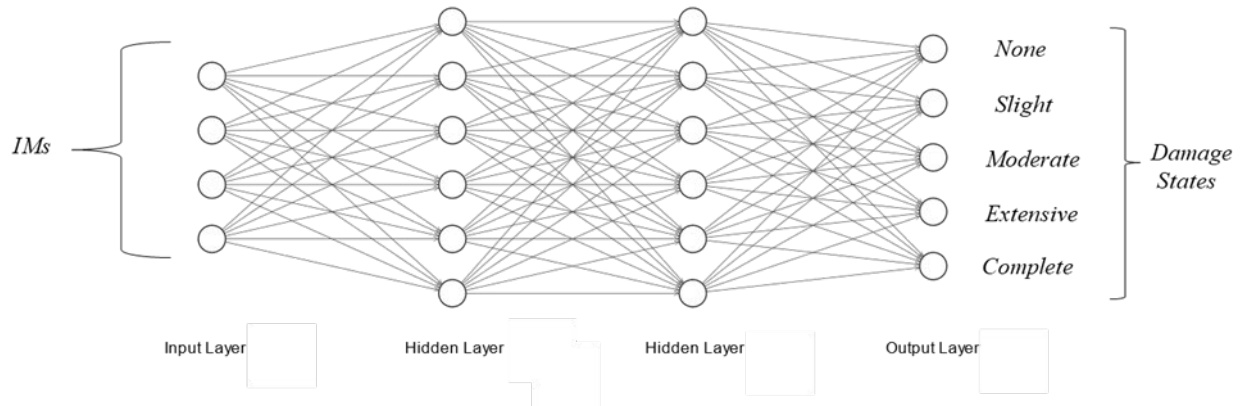


Figure 5.1 The architecture of the ANN seismic classifier using IMs as inputs and damage states resulted from NLTHA as output

$$\sigma_1(s) = \sigma_2(s) = \begin{cases} 0 & \text{if } s \leq 0 \\ s & \text{if } s > 0 \end{cases} \quad (5.1)$$

$$\sigma_3(s) = \left\{ \frac{e^{s_i}}{\sum_{k=1}^J e^{s_k}} \right\}, i = 1, 2, \dots, J, \text{ where } J \text{ is the length of vector } s \quad (5.2)$$

The process of using IMs inputs to predict damage states is outlined in the following steps:

**Step 1** involves the vector  $X = \{1, x_1, x_2, \dots, x_N\}$  where 1 denotes the bias item and  $x_i$  are the IMs inputs.

In **Step 2**, vector  $X$  is propagated through the hidden layer  $L_1$  to produce a new vector, as shown in equation (5.3). The elements of  $a^{L1}$  pass through activation function  $\sigma_1$  generating another vector as described in equation (5.4), which then serves as input for the hidden layer  $L_2$ .

$$a^{L1} = W^{L1} X^T \quad (5.3)$$

$$Z^{L1} = \{1, \sigma_1(a^{L1})\} \quad (5.4)$$

**Step 3** follows a similar procedure to Step 2, resulting in an output generated from the hidden layer  $L_2$  as shown in equation (5.5).

$$Z^{L2} = \{1, \sigma_2(a^{L2})\} \quad (5.5)$$

**Step 4**, a vector described in equation (x) and its corresponding activation function are computed. The vector  $Z^{L3}$  consists of five elements representing the predicted probabilities for each damage state. The final prediction for the damage state is determined by selecting the state with the highest probability prediction.

$$Z^{L3} = \sigma_3(a^{L3}) \quad (5.6)$$

The effectiveness of ANN seismic classifiers hinges significantly upon two key factors: synaptic weights and activation functions, which govern how information flows through the ANN architecture. For the hidden layers, ReLU was chosen due to its computational efficiency and ability to converge effectively (Krizhevsky, Sutskever, and Hinton 2017). Meanwhile, the SoftMax activation function, widely recognized for its utility in multiclassification tasks (Gao and Pavel 2017), was implemented in the output layer.

Optimal synaptic weights are crucial and are refined through ANN training to maximize performance. Initially, a comprehensive collection of ground motion records is assembled as training samples. Corresponding damage states incurred by these records are determined through NLTHA, serving as ground-truth data. Subsequently, the IMs from these training samples are fed into the ANN classifier to predict the associated damage states. Comparison between the ANN-predicted states and the ground-truth states facilitates calculation of the classification error, typically assessed using cross-entropy loss (Pang et al. 2019), as displayed in equation (5.7)

$$E = - \sum_{k=1}^J y_k \ln (Z_{L_s}) \quad (5.7)$$

The classification error  $E$ , defined in equation (5.7), quantifies discrepancies between predicted and actual damage states. Here,  $y_k$  denotes the label of the  $k - th$  damage state, and  $Z_k^{L3}$  represents the output derived in Step 4, contingent upon input  $X$  and the adjustable synaptic



weights  $W$ . The minimization of  $E$  is achieved through backpropagation from the output layer to the initial hidden layer, leveraging the gradient  $\partial W \frac{\partial E(X,W)}{\partial W}$  via the Chain rule.

During backpropagation, the trainable weights are updated iteratively using equation (5.8), which incorporates a small positive value  $\eta$ , referred to as the learning rate. This process follows a basic gradient descent optimization algorithm, though advanced optimization techniques are also available in current literature (Ruder 2016).

$$W^{new} = W^{old} - \eta \frac{\partial E(X, W)}{\partial W} \quad (5.8)$$

Training continues iteratively, with the ANN classifier processing training samples until it achieves optimal performance, typically indicated by the lowest classification error on a distinct test dataset, is achieved. At this point, the training process concludes.

The (ANN) classifier undergoes an iterative training process using the training subset to compute gradients and update weights as specified in equation (5.8). Performance monitoring of the ANN is conducted with the validation subset. Overfitting is identified when the validation error increases while the training error decreases, signaling that training should be halted to ensure optimal ANN performance. Overfitting results in diminished performance on new, unseen data such as future ground motions. The test subset also plays a role in monitoring the model's training. A significant discrepancy between the minimum test error and the validation error suggests an improper division of training samples, necessitating a potential retraining of the ANN classifier. The ANN training employs the scaled conjugate gradient (SCG) backpropagation algorithm (Møller 1993). The training process is controlled by six key parameters: epochs, goal, time, learning rate ( $lr$ ),  $min\_grad$ , and  $max\_fail$ . Specifically, epochs refer to the maximum number of epochs for training, where one epoch means all samples

in the training subset are used once for training; the goal represents the desired performance objective;  $lr$  is the learning rate; time denotes the maximum training duration in seconds;  $min\_grad$  is the minimum performance gradient; and  $max\_fail$  indicates the maximum number of allowable validation failures. In this study, the learning rate ( $lr$ ) is set at 0.001, and training stops when any of the following conditions are met: epochs reach 1,000, the goal is achieved,  $min\_grad$  drops to  $10^{-6}$ , or  $max\_fail$  reaches 10.

### 5.2 Classification model (A)

As outlined in Section 4.1, two methods were employed to distinguish the collapse damage state, resulting in two distinct datasets. Model (A) includes 788 ground motion records per damage class, totaling 3,940 records. Of this, 90% was allocated for training, while 10% was reserved for validation, and another 10% for testing. This distribution translates to 3,150 points for training, 395 points for validation, and 395 points for testing. The specifics are illustrated in Figure 5.2.

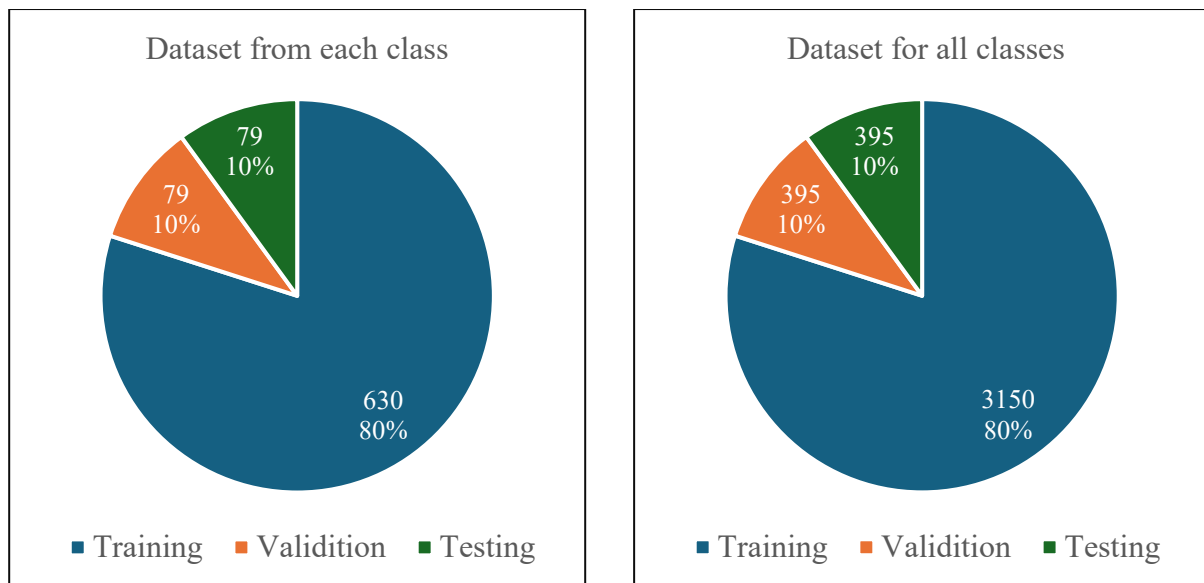


Figure 5.2 Details of the data used in Model (A) showing training, validation, and testing datasets.

In Figure 5.3, the classification performance of a seismic classifier is illustrated using the training, validation, and testing datasets, as well as a combined dataset. The rows of the confusion matrix represent the predicted classes (output classes), while the columns represent the actual classes (target classes). Green cells indicate matches between predicted and actual classes, whereas red cells denote mismatches.

For instance, within the training dataset, 604 out of 630 ground motions were correctly classified as 'none', while 26 ground motions were incorrectly predicted as 'slight damage' when actually belonging to the 'none' class. Each cell's percentage reflects its proportion of the total number of datasets. The last column of each row shows the prediction accuracies in percentages, and the bottom right cell indicates the overall accuracy for the dataset.

The training set accuracy stands at 91.21%, the validation set at 90.63%, and the testing set at 87.09%. The combined overall accuracy is 90.74%. The similarity in accuracy across the three datasets and the combined dataset indicates that there is no significant overfitting in this ANN classifier model. The slight difference between the training set accuracy (91.21%) and the testing set accuracy (87.09%) confirms this, as the difference is minimal.

None	604 19.17%	26 0.83%	0 0.0%	0 0.0%	0 0.0%	95.87% 4.13%
Slight	20 0.63%	568 18.03%	42 1.33%	0 0.0%	0 0.0%	90.16% 9.84%
Moderate	0 0.0%	45 1.43%	567 18.0%	17 0.54%	1 0.03%	90.0% 10.0%
Extensive	0 0.0%	1 0.03%	15 0.48%	573 18.19%	41 1.30%	90.95% 9.05%
Collapse	0 0.0%	0 0.0%	1 0.03%	68 2.16%	561 18.9%	89.05% 10.95%
(Output Class)	96.79% 3.21%	88.75% 11.25%	90.72% 9.28%	87.08% 12.92%	93.03% 6.97%	91.21% 8.79%
	None	Slight	Moderate	Extensive	Collapse	(Target Class)

(Training dataset)

None	75 18.99%	4 1.01%	0 0.0%	0 0.0%	0 0.0%	94.94% 5.06%
Slight	1 0.25%	75 18.99%	3 0.76%	0 0.0%	0 0.0%	94.94% 5.06%
Moderate	0 0.0%	10 2.53%	65 16.46%	4 1.01%	0 0.0%	82.28% 17.72%
Extensive	0 0.0%	0 0.0%	1 0.25%	73 18.48%	5 1.27%	92.41% 7.59%
Collapse	0 0.0%	0 0.0%	1 0.25%	8 2.03%	70 17.72%	89.05% 10.95%
(Output Class)	98.68% 1.32%	84.27% 15.73%	92.86% 7.14%	85.88% 14.12%	93.33% 6.67%	90.63% 9.37%
	None	Slight	Moderate	Extensive	Collapse	(Target Class)

(Validation dataset)

None	74 18.73%	5 1.27%	0 0.0%	0 0.0%	0 0.0%	93.67% 6.33%
Slight	7 1.77%	67 16.96%	5 1.27%	0 0.0%	0 0.0%	84.81% 15.19%
Moderate	0 0.0%	6 1.52%	73 18.48%	0 0.0%	0 0.0%	92.41% 7.59%
Extensive	0 0.0%	0 0.0%	4 1.01%	64 16.20%	11 16.71%	81.01% 18.99%
Collapse	0 0.0%	0 0.0%	1 0.25%	12 3.04%	66 16.71%	83.54% 16.46%
(Output Class)	91.36% 8.64%	85.90% 14.10%	87.95% 12.05%	84.21% 15.79%	85.71% 14.29%	87.09% 12.91%
	None	Slight	Moderate	Extensive	Collapse	(Target Class)

(Testing dataset)

None	753 19.11%	35 0.89%	0 0.0%	0 0.0%	0 0.0%	95.56% 4.44%
Slight	28 0.71%	710 18.02%	50 1.27%	0 0.0%	0 0.0%	90.10% 9.90%
Moderate	0 0.0%	61 1.55%	705 17.89%	21 0.53%	1 0.03%	89.47% 10.53%
Extensive	0 0.0%	1 0.03%	20 0.51%	710 18.02%	57 1.45%	90.10% 9.90%
Collapse	0 0.0%	0 0.0%	3 0.08%	88 2.23%	697 17.69%	88.45% 11.55%
(Output Class)	96.41% 3.59%	87.98% 12.02%	90.62% 9.38%	86.69% 13.31%	92.32% 7.68%	90.74% 9.26%
	None	Slight	Moderate	Extensive	Collapse	(Target Class)

(Combined dataset)

Figure 5.3 Confusion matrices of Model (A) where green and red cells are the percentages of right and wrong classifications in the current subset.

### 5.3 Classification model (B)

Model (B) is comprised of 3,049 ground motion records for each damage class, resulting in a total of 15,245 records. The dataset was divided randomly such that 90% was designated for training, and 10% each for validation and testing. This allocation corresponds to 12,195 training points, 1,525 validation points, and 1,525 testing points. Detailed information is provided in Figure 5.4.

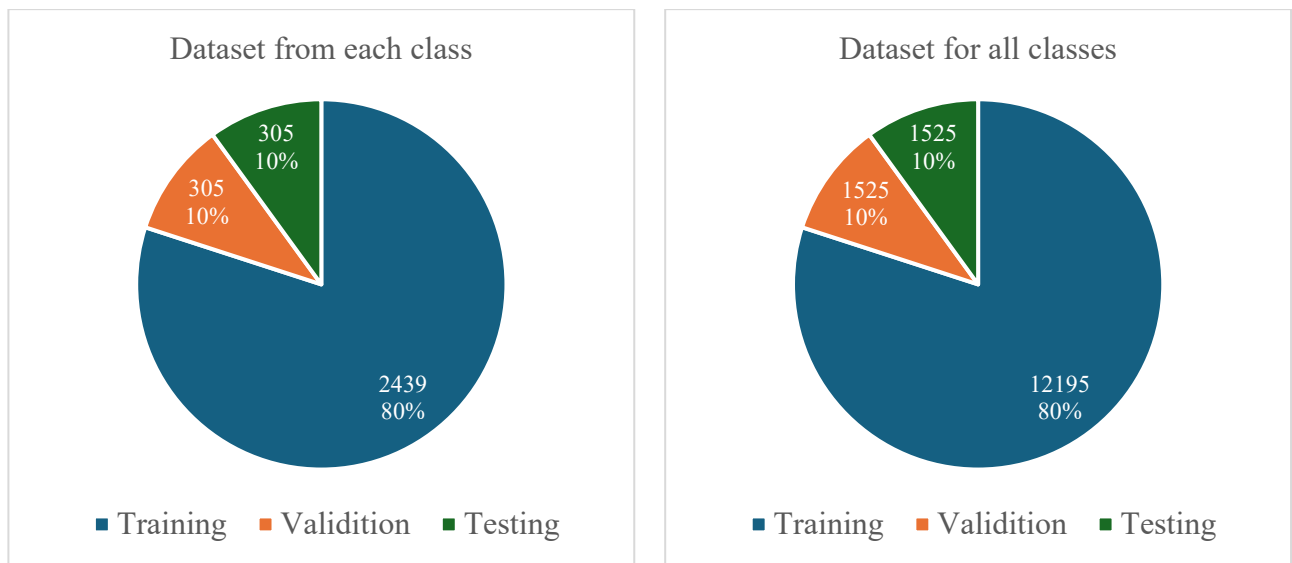


Figure 5.4 Details of the data used in Model (B) showing training, validation, and testing datasets.

Figure 5.5 presents the confusion matrices for Model B, adhering to the same conventions as Model A concerning colors, order, and percentages. The training set accuracy sets at 96.18%, the validation set at 93.15%, and the testing set at 91.41%. The combined overall accuracy is 95.43%. Notably, Model B demonstrates higher prediction accuracy across all datasets compared to Model A. This improvement is attributed to the substantially larger dataset

used for Model B, which includes 15,245 ground motion records, in contrast to Model A's 3,940 records.

At the class level, Model B shows significantly higher accuracy for the 'none' and 'collapse' states. This is because these classes are 'open classes', meaning they have only one boundary limit. With a larger dataset, the accuracy of open classes improves significantly since there is just one limit to consider, unlike other classes that have two limits.

Moreover, the criteria for classifying and differentiating between 'extensive' and 'collapse' states vary between Model B and Model A, influencing their performance. In Model A, collapse states were determined based on the maximum drift ratio from pushover analysis. In contrast, Model B classified collapse states based on a 20% loss and degradation of overall stiffness. This difference in classification criteria leads to variations in behavior and results. Additionally, the ground motions selected for Model A were not consistently strong enough to always result in a collapse classification, introducing minor uncertainties and differing outcomes based on the classification methodology.

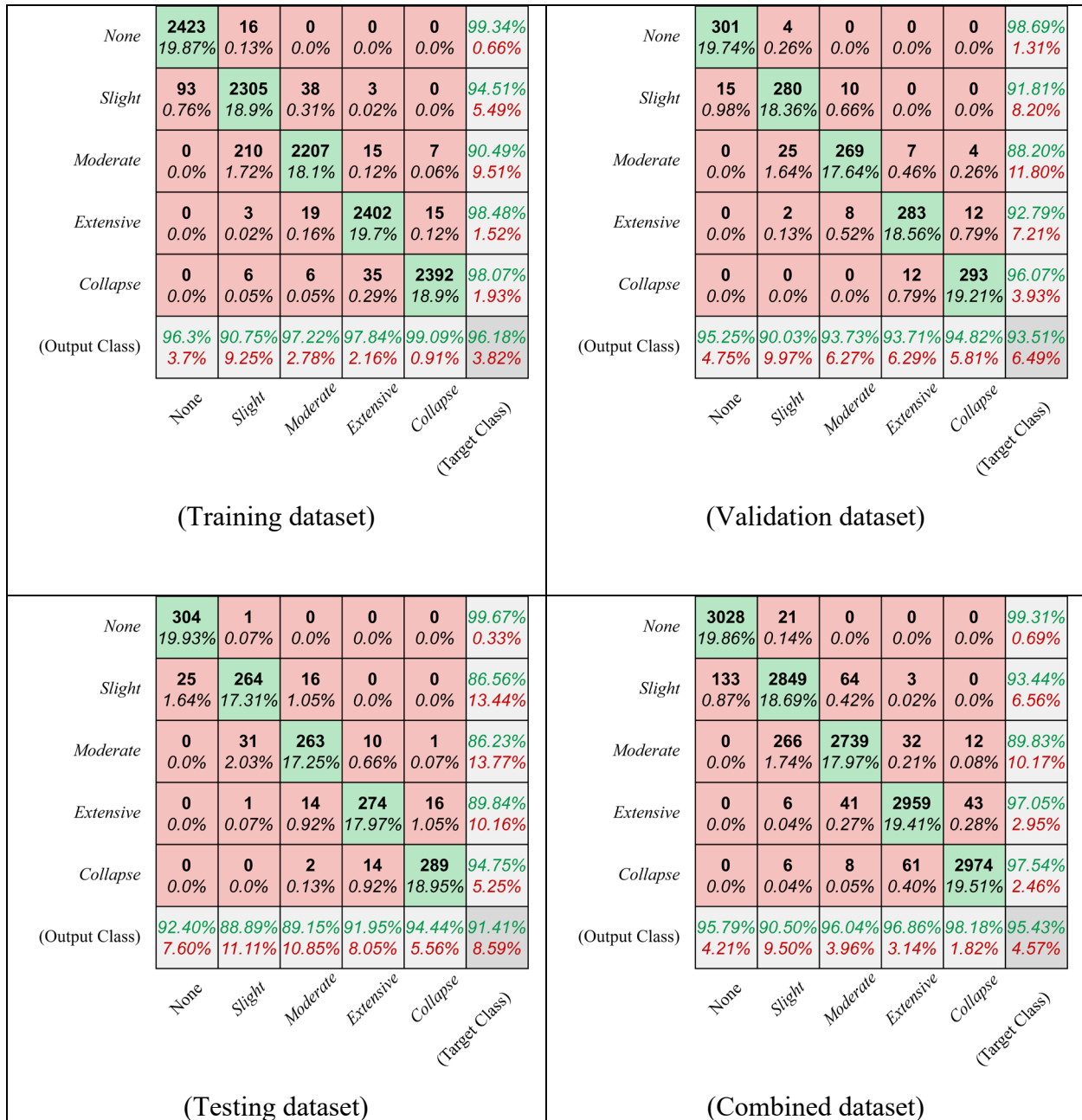


Figure 5.5 Confusion matrices of Model (B) where green and red cells are the percentages of right and wrong classifications in the current subset.

## Chapter 6 Conclusions

The proposed ANN-based classifier offers a new, rapid, and accurate method for damage estimation, surpassing traditional fragility estimations. This model uses intensity measures as inputs to predict damage classes for two selected steel girder highway bridges in southeast Missouri, and its predictions are compared with actual damage classifications obtained from nonlinear time history analysis.

Two models were developed: Model A and Model B. Model A achieved an overall accuracy of 90.74%, while Model B achieved a higher overall accuracy of 95.43%. This improvement is attributed to the larger dataset size and refined criteria for classifying the collapse state in Model B.

Compared to the fragility analysis, the ANN damage classifier results are promising, demonstrating high accuracy in damage estimation. The proposed methodology for developing an ANN seismic classifier is applicable to various types of structures. Future studies could extend this approach to different bridge types, such as suspended bridges or concrete beam bridges, potentially aiding in better city planning and enhancing infrastructure health systems.



## References

- A, Gautham., and K. Gopi Krishna. 2017. "Fragility Analysis – A Tool to Assess Seismic Performance of Structural Systems." *Materials Today: Proceedings* 4 (9): 10565–69. <https://doi.org/10.1016/j.matpr.2017.06.421>.
- Bridle, John S. 1990. "Probabilistic Interpretation of Feedforward Classification Network Outputs, with Relationships to Statistical Pattern Recognition." In *Neurocomputing*, 227–36. Berlin, Heidelberg: Springer Berlin Heidelberg. [https://doi.org/10.1007/978-3-642-76153-9\\_28](https://doi.org/10.1007/978-3-642-76153-9_28).
- Bridle, John. "Training stochastic model recognition algorithms as networks can lead to maximum mutual information estimation of parameters." *Advances in neural information processing systems* 2 (1989).
- Buckle, I. "The Northridge, California earthquake of January 11, 1994: performance of highway bridges." Tech. Rep. NCEER-94-0068 (1994).
- Chen, G, Pe N Anderson, Pe R Luna, Pe R Stephenson, Pe M El-Engebawy, P Silva, and Pe R Zoughi. 2005. "EARTHQUAKE HAZARDS ASSESSMENT AND MITIGATION: A PILOT STUDY IN THE NEW MADRID SEISMIC ZONE." <http://www.cies.umr.edu/>.
- Ciano, M., M. Giofrè, and M. Grigoriu. 2020. "The Role of Intensity Measures on the Accuracy of Seismic Fragilities." *Probabilistic Engineering Mechanics* 60 (April):103041. <https://doi.org/10.1016/j.probengmech.2020.103041>.
- Cooper, James, and I. Friedland. "The Northridge earthquake: Progress made, lessons learned..." *Public Roads* 58, no. 1 (1994): 26-36.
- Elghazouli, A. Y., M. Kumar, and P. J. Stafford. 2014. "Prediction and Optimisation of Seismic Drift Demands Incorporating Ground Motion Frequency Content." *Bulletin of Earthquake Engineering* 12 (1): 255–76. <https://doi.org/10.1007/s10518-013-9568-7>.
- Emergency Management Agency, Federal. 2022. "Hazus 5.1 Earthquake Model User Guidance."
- Gao, Bolin, and Laca Pavel. "On the properties of the softmax function with application in game theory and reinforcement learning." arXiv preprint arXiv:1704.00805 (2017).
- Hall, Mark A. "Correlation-based feature selection for machine learning." PhD diss., The University of Waikato, 1999.
- Hall, Mark A., and Lloyd A. Smith. "Feature selection for machine learning: comparing a correlation-based filter approach to the wrapper." In *Proceedings of the twelfth international Florida artificial intelligence research society conference*, pp. 235-239. 1999.
- Haykin, Simon. *Neural networks and learning machines*, 3/E. Pearson education india, 2009.

- Kafali, Cagdas, and Mircea Grigoriu. 2007. "Seismic Fragility Analysis: Application to Simple Linear and Nonlinear Systems." *Earthquake Engineering & Structural Dynamics* 36 (13): 1885–1900. <https://doi.org/10.1002/eqe.726>.
- Karamlou, Aman, and Paolo Bocchini. 2015. "Computation of Bridge Seismic Fragility by Large - scale Simulation for Probabilistic Resilience Analysis." *Earthquake Engineering & Structural Dynamics* 44 (12): 1959 - 78. <https://doi.org/10.1002/eqe.2567>.
- Kostinakis, Konstantinos, Asimina Athanatopoulou, and Konstantinos Morfidis. 2015. "Correlation between Ground Motion Intensity Measures and Seismic Damage of 3D R/C Buildings." *Engineering Structures* 82 (January):151–67. <https://doi.org/10.1016/j.engstruct.2014.10.035>.
- Krizhevsky, Alex, Ilya Sutskever, and Geoffrey E. Hinton. 2017. "ImageNet Classification with Deep Convolutional Neural Networks." *Communications of the ACM* 60 (6): 84–90. <https://doi.org/10.1145/3065386>.
- Kunnath SK, Reinhorn AM, et al. (1992) IDARC Version 3: A program for the inelastic damage analysis of RC structures, Technical report NCEER-92-0022. National center for earthquake engineering research, State University of New York, Buffalo
- Lok, T. M. (1999). "Effect of soil nonlinearity to the behavior of seismic soil-pile-structure interaction," Ph.D. dissertation, University of California, Berkeley, California.
- Luco, Nicolas, and Paolo Bazzurro. 2007. "Does Amplitude Scaling of Ground Motion Records Result in Biased Nonlinear Structural Drift Responses?" *Earthquake Engineering & Structural Dynamics* 36 (13): 1813–35. <https://doi.org/10.1002/eqe.695>.
- Mangalathu, Sujith, Gwanghee Heo, and Jong-Su Jeon. 2018. "Artificial Neural Network Based Multi-Dimensional Fragility Development of Skewed Concrete Bridge Classes." *Engineering Structures* 162 (May):166–76. <https://doi.org/10.1016/j.engstruct.2018.01.053>.
- Matlock, Hudson. 1970. "Correlation for Design of Laterally Loaded Piles in Soft Clay." In *All Days*. OTC. <https://doi.org/10.4043/1204-MS>.
- Miano, Andrea, Fatemeh Jalayer, Hossein Ebrahimian, and Andrea Prota. 2018. "Cloud to IDA: Efficient Fragility Assessment with Limited Scaling." *Earthquake Engineering & Structural Dynamics* 47 (5): 1124–47. <https://doi.org/10.1002/eqe.3009>.
- Møller, Martin Fodslette. 1993. "A Scaled Conjugate Gradient Algorithm for Fast Supervised Learning." *Neural Networks* 6 (4): 525–33. [https://doi.org/10.1016/S0893-6080\(05\)80056-5](https://doi.org/10.1016/S0893-6080(05)80056-5).
- Nair V, Hinton GE. Rectified linear units improve Restricted Boltzmann machines. In: *ICML 2010 - Proceedings, 27th int. conf. mach. learn.*, 2010.
- Padgett, Jamie E., Bryant G. Nielson, and Reginald DesRoches. 2008. "Selection of Optimal Intensity Measures in Probabilistic Seismic Demand Models of Highway Bridge Portfolios."

- Earthquake Engineering & Structural Dynamics 37 (5): 711–25.  
<https://doi.org/10.1002/eqe.782>.
- Pang, Tianyu, Kun Xu, Yinpeng Dong, Chao Du, Ning Chen, and Jun Zhu. "Rethinking softmax cross-entropy loss for adversarial robustness." arXiv preprint arXiv:1905.10626 (2019).
- Park, Y. J., A. H-S. Ang, and Y. K. Wen. 1987. "Damage-Limiting Aseismic Design of Buildings." *Earthquake Spectra* 3 (1): 1–26. <https://doi.org/10.1193/1.1585416>.
- Park, Young - Ji, and Alfredo H. - S. Ang. 1985. "Mechanistic Seismic Damage Model for Reinforced Concrete." *Journal of Structural Engineering* 111 (4): 722 – 39.  
[https://doi.org/10.1061/\(ASCE\)0733-9445\(1985\)111:4\(722\)](https://doi.org/10.1061/(ASCE)0733-9445(1985)111:4(722)).
- Rathje, Ellen M., Fadi Faraj, Stephanie Russell, and Jonathan D. Bray. 2004. "Empirical Relationships for Frequency Content Parameters of Earthquake Ground Motions." *Earthquake Spectra* 20 (1): 119–44. <https://doi.org/10.1193/1.1643356>.
- Riddell, Rafael. 2007. "On Ground Motion Intensity Indices." *Earthquake Spectra* 23 (1): 147–73. <https://doi.org/10.1193/1.2424748>.
- Román-De La Sancha, A., J.M. Mayoral, T.C. Hutchinson, G. Candia, J. Montgomery, and S. Tepalcapa. 2019. "Assessment of Fragility Models Based on the Sept 19th, 2017 Earthquake Observed Damage." *Soil Dynamics and Earthquake Engineering* 125 (October):105707.  
<https://doi.org/10.1016/j.soildyn.2019.105707>.
- Ruder, Sebastian. "An overview of gradient descent optimization algorithms." arXiv preprint arXiv:1609.04747 (2016).
- Sontag, E.D. 1992. "Feedback Stabilization Using Two-Hidden-Layer Nets." *IEEE Transactions on Neural Networks* 3 (6): 981–90. <https://doi.org/10.1109/72.165599>.
- Vamvatsikos, Dimitrios, and C. Allin Cornell. 2002. "Incremental Dynamic Analysis." *Earthquake Engineering & Structural Dynamics* 31 (3): 491–514.  
<https://doi.org/10.1002/eqe.141>.
- Yasmin, Tarannum, Ajay Chourasia, S K Bhattacharyya, and Jalaj Parashar. 2015. "FRAGILITY ANALYSIS FOR SEISMIC VULNERABILITY ASSESSMENT OF BUILDINGS: A REVIEW." *International Research Journal of Engineering and Technology*. [www.irjet.net](http://www.irjet.net).
- Yuan, Xinzhe, Genda Chen, Pu Jiao, LiuJun Li, Jun Han, and Haibin Zhang. 2022. "A Neural Network-Based Multivariate Seismic Classifier for Simultaneous Post-Earthquake Fragility Estimation and Damage Classification." *Engineering Structures* 255 (March).  
<https://doi.org/10.1016/j.engstruct.2022.113918>.